Evidence of Two-Source King Plot Nonlinearity in Spectroscopic Search for New Boson:
Supplemental Material

Joonseok Hur,[1,*] Diana P. L. Aude Craik,[1,*] Ian Counts,[1,*] Eugene Knyazev,[1] Luke Caldwell,[2]
Calvin Leung,[1] Swadha Pandey,[1] Julian C. Berengut,[3] Amy Geddes,[3] Witold Nazarewicz,[4]
Paul-Gerhard Reinhard,[5] Akio Kawasaki,[6] Honggi Jeon,[7] Wonho Jhe,[7] and Vladan Vuletić[1,†]

[1] *Department of Physics and Research Laboratory of Electronics,*
Massachusetts Institute of Technology, Cambridge, Massachusetts 02139, USA
[2] *JILA, NIST and University of Colorado, Boulder, Colorado 80309, USA*
[3] *School of Physics, University of New South Wales, Sydney, New South Wales 2052, Australia*
[4] *Facility for Rare Isotope Beams and Department of Physics and Astronomy,*
Michigan State University, East Lansing, Michigan 48824, USA
[5] *Institut für Theoretische Physik, Universität Erlangen, Erlangen D-91054, Germany*
[6] *National Metrology Institute of Japan (NMIJ), National Institute of Advanced Industrial Science and Technology (AIST),*
1-1-1 Umezono, Tsukuba, Ibaraki 305-8563, Japan
[7] *Department of Physics and Astronomy, Seoul National University, Seoul 151-747, Korea*

I. EXPERIMENTAL DETAILS

Fig. S1 shows the relevant transitions of Yb$^+$, with the narrow transitions used for isotope shift measurements depicted in blue. In this work, we probe the 467-nm transition and combine our measurements with our previous data on isotope shifts on the 411 nm and 435 nm transitions from Ref. [1], as well as data from transitions in neutral Yb from Refs. [2, 3]. We Doppler-cool the trapped ion (see Fig. S2) to $\sim 500\mu$K using 369-nm light which, aided by repumpers at 935 nm and 760 nm, drives a cycling transition between the $^2S_{1/2}$ and $^2P_{1/2}$ levels. Here we also report for the first time the frequencies (for all stable even isotopes) of the 760 nm-transition which is used to repump the ion from the $^2F_{7/2}$ state (see Table S1 and Sec. I A). The frequencies of the cooling transition at 370 nm and the repumping transition for the $^2D_{3/2}$ state at 935 nm for ^{168}Yb$^+$ can be found in Table S1 as well.

To produce 467 nm probe light, we frequency-double a Ti:Sapphire laser at 934 nm with an M Squared ECD-X external cavity doubler. As described in detail in Ref. [1], we divert some of the light before the doubling cavity and pass it through an electro-optic modulator (EOM) to produce a sideband several gigahertz away from the carrier. We frequency-stabilize this sideband to a ultralow-thermal-expansion (ULE) high-finesse cavity using the Pound-Drever-Hall (PDH) protocol. Coarse frequency tuning of the probe light is then achieved simply by scanning the sideband frequency. Fine-tuning of the probe frequency is accomplished with an acousto-optic modulator (AOM) for the frequency-doubled light. Our probe beam power is 160 mW and an achromatic lens is used to focus the beam to a waist ($1/e^2$-intensity radius) of 15 μm at the ion.

To determine the center of the 467 nm transition, we drive two transitions, labeled R and B in Fig. S1(b), between symmetrically red and blue-detuned Zeeman components of the $^2S_{1/2}$ and $^2F_{7/2}$ states, and average their center frequencies. To minimize the effect of magnetic-field drifts, we interleave the scans of R and B (i.e. we record one data point on the frequency scan of R, then shift the frequency of the probe laser and take a data point on the frequency scan of B, then take another point on the scan of R and so on). A 0.5 s pause time is used after shifting the frequency between the R and B transitions to allow the laser to settle.

Fig. S3 shows the 500 ms-long laser pulse sequence used to drive the 467 nm transition, and Fig. S2 depicts the polarization and propagation direction of the laser beams. The sequence begins by cooling the ion with 369 nm light and optically pumping it with a circularly-polarized 369 nm-beam to one of the two $m_s = \pm\frac{1}{2}$ levels of the $^2S_{1/2}$ ground state. We record fluorescence emitted during cooling to confirm that the ion has been correctly initialized to the ground state and has not been shelved to one of the long-lived D or F states. (If the ion goes dark during this time, the corresponding period of the sequence is ignored in the data.) A probe laser pulse is then applied for 390 ms, followed by readout of fluorescence by electron shelving [1, 4]. During readout, the 369 nm-cooling light is again applied. When the transition has occurred, the ion will be in the $F_{7/2}$ state and will not fluoresce when illuminated by the cooling light. In this case, we consider the ion to have performed a quantum jump. However, if the ion did not make the transition and remained in the ground state, it will emit fluorescence on the cycling transition when driven by the cooling light. For each point on a frequency scan of the probe laser, we repeat this sequence until 10 successful

---

[*] These authors contributed equally to this work.
[†] vuletic@mit.edu

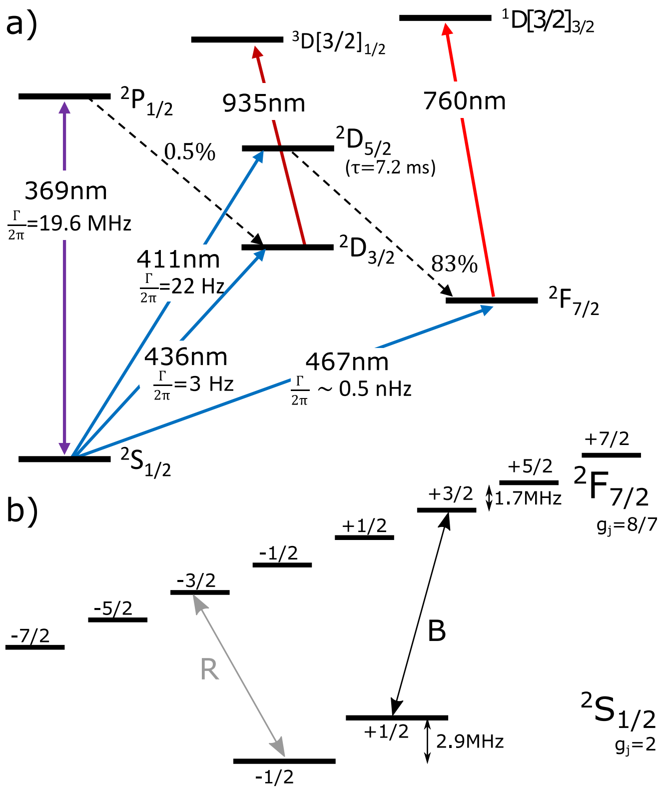

FIG. S1. (a) Partial level diagram for the Yb$^+$ ion. In this work, we measure the 467-nm transition and use our previous measurements of the 411-nm and 436-nm transitions [1] to produce the King plots. (b) Zeeman levels of the ground $^2S_{1/2}$ and excited $^2F_{7/2}$ states of the 467-nm transition. We use a static magnetic field $B_0 = 1.05\,\mathrm{G}$ to split the Zeeman levels.

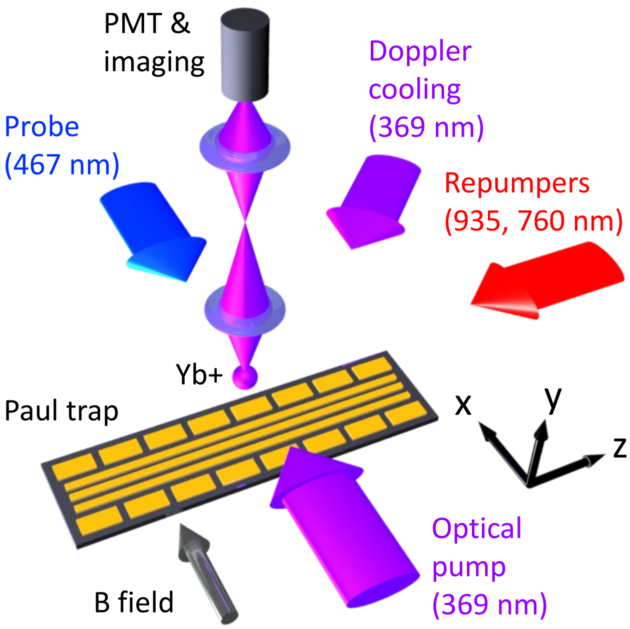

FIG. S2. Schematic drawing of the experimental setup. A single ytterbium ion is trapped 135 μm away from the surface of a microfabricated planar Paul trap housed in an ultrahigh vacuum chamber. The propagation directions of the laser beams used for cooling, repumping, optical pumping, and probing the ion are indicated by labeled arrows. Fluorescence from the ion is collected using either a photo-multiplier tube (PMT) or a camera. The probe laser beam is linearly polarized along the trap axis (the z direction in this figure).

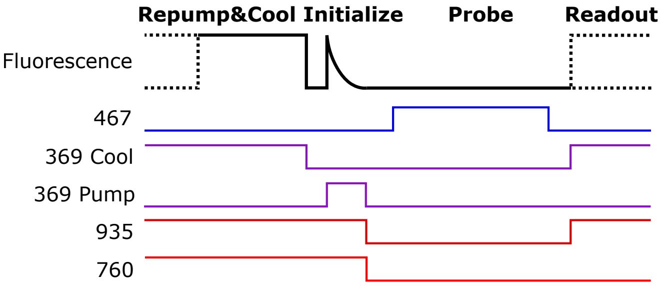

FIG. S3. Time sequence of the experiment with wavelengths of lasers indicated.

periods of the sequence (i.e., the periods staring with the ion in the ground state) are observed, and determine what fraction of attempts resulted in a quantum jump. Fig. S4 shows the quantum jump probability versus probe laser frequency for one frequency scan.

We measure isotope shifts between pairs of isotopes by loading individual ions of each isotope in turn into the trap. (We can selectively photoionize different isotopes by tuning the frequency of our 399 nm photoionization laser.) For a given trapped isotope, we take at least 7 simultaneous frequency scans of the R and B Zeeman transitions before switching to the other isotope. This process is repeated at least four times throughout the course of a day of data taking (i.e., four data segments for each isotope). We calculate the common frequency drift for each pair of scans R and B to determine the center frequency, see Fig. S5(a). We then fit this data using a least-squares fit with varying offset [see the Supplemental Material of Ref. [1], Eq. (S1)]. As described in detail in Sec. II C, we measured all seven possible combinations of nearest-even-neighbor $(A, A+2)$ and next-to-nearest-even-neighbor isotope pairs $(A, A+4)$ in order to cross-check our measurement results for systematic errors, and to improve our precision.

A. Repumping from the $^2D_{3/2}$ and $^2F_{7/2}$-states

The state $^2F_{7/2}$ state is repumped by a 760 nm laser beam that drives the $2F_{7/2} \rightarrow {}^1D[3/2]_{3/2}$ transition [5–10] with a $\lesssim$ 10-ms time constant for a $\sim$ 7 mW beam focused to a waist of 100 μm (consistent with Refs. [5, 6]). The absolute frequency of the 760 nm beam is measured by and actively stabilized to a Fizeau wavemeter (HighFinesse/Ångstrom WS/7). The frequencies for this

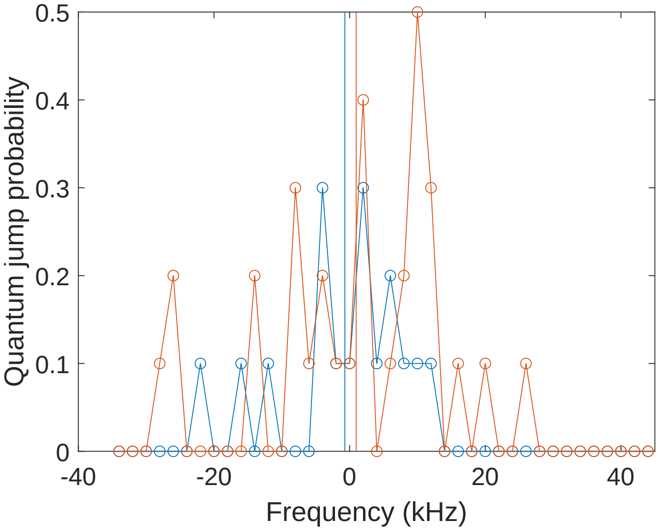

FIG. S4. Example of simultaneous frequency scans of the probe transition on the R and B Zeeman components. Here the horizontal axis has been offset so that the Zeeman splitting is not shown. Vertical lines correspond to the statistical mean value for the frequency for each peak.

transition for all the isotopes, as well as the frequencies for the ${}^2D_{3/2} \rightarrow {}^3D[3/2]_{1/2}$ repumping transition at 935 nm, are shown in Table S1.

II. DATA ANALYSIS

A. Determining the transition center frequency

As described in Sec. I, for each isotope, we determine the ${}^2S_{1/2} \rightarrow {}^2F_{7/2}$ transition center frequency by driving two symmetrically detuned transitions between Zeeman levels of the ground and excited states, transitions R and B [see Fig. S1(b)], and averaging their center frequencies. We scan the probe laser frequency and plot the quantum jump probability versus frequency, see Fig. S4. To determine the center frequencies of R and B from our data, we take the statistical mean of our data points. This allows us to determine the center frequency without assuming a known lineshape fit function. However, this method of determining the center is susceptible to a small amount of frequency pulling if our scan range is not centered at the transition resonance frequency (we discuss this effect in detail in Sec. III G and determine that it is significantly smaller than our leading error sources). An analysis where we fit lineshapes Gaussian function with background offset to find the transition centers gives deviations that are smaller than our statistical error bars.

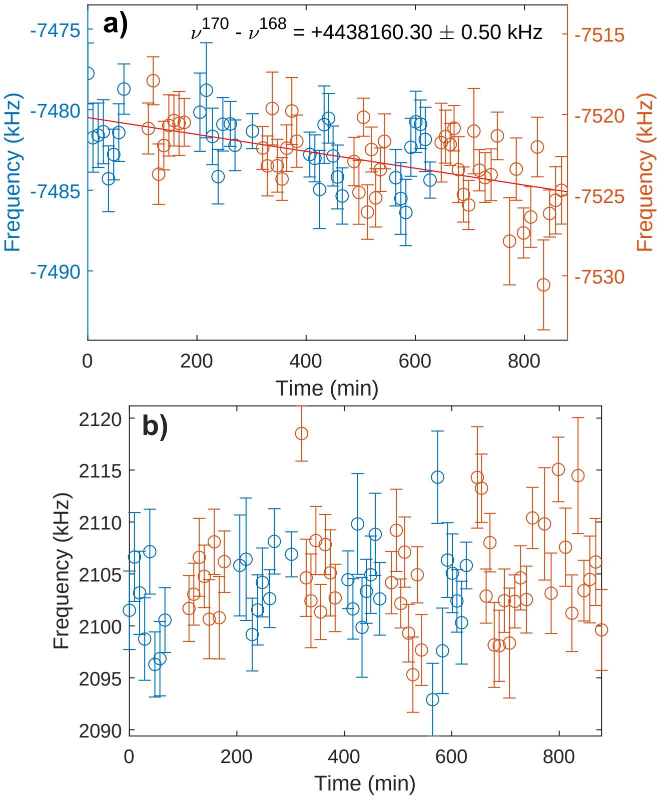

FIG. S5. (a) Example of the common frequency drift of Zeeman peaks R and B for the IS measurement. Linear fit follows the drift of the ULE cavity frequency reference. Orange and blue color correspond to ${}^{168}\mathrm{Yb}^+$ and ${}^{170}\mathrm{Yb}^+$, respectively. (b) Example of the frequency difference between the Zeeman peaks R and B. The Zeeman splitting is affected by variations of the external magnetic field, but not by the drifts of the ULE cavity.

B. Inverse-mass difference $\mu^{AA'}$

Assuming that the errors of the measured masses of all five isotopes of interest are uncorrelated, we calculate the inverse-mass differences $\mu^{AA'} = 1/m^A - 1/m^{A'}$ (where m^A is the mass of the ${}^A\mathrm{Yb}^+$ ion) and the correlations between different $\mu^{AA'}$ for different isotope pairs (A, A'). The values for m^A, $\mu^{AA'}$, and their correlations, are listed in Table S2, Table I in the main text, and Table S3, respectively.

The uncertainties in measured atomic masses of Yb isotopes appear as x-errors in frequency-normalized King plots [see Eq. (2) in the main text]. The effect of mass uncertainties is largely suppressed due to the small slopes in King plots (given by $K_{\kappa\chi}$, the two-transition mass shift coefficients). The maximum uncertainty in measured Yb masses m^A is currently 10^{-7} u (limited by the ^{168}Yb isotope), translating into an uncertainty of $3.6 \times 10^{-12}\,\mathrm{u}^{-1}$ in $\mu^{AA'}$ (see Table S2 and Table I in the main text). This mass uncertainty leads to a 22 Hz uncertainty in $K_{\kappa\chi}\mu^{AA'}$, for the maximum value of $K_{\kappa\chi} = 6002\,\mathrm{GHz{\cdot}u}$

TABLE S1. Measured values of absolute frequencies ν^A (upper table) and isotope shifts $\nu^{AA'} = \nu^A - \nu^{A'}$ (lower table) for the ${}^2S_{1/2} \to {}^2P_{1/2}$ (369 nm) cooling transition, and the ${}^2D_{3/2} \to {}^3D[3/2]_{1/2}$ (935 nm) and ${}^2F_{7/2} \to {}^1D[3/2]_{3/2}$ (760 nm) repumping transitions. 100 MHz, 60 MHz, and 50 MHz uncertainties in measured absolute frequencies of the 369 nm, 760 nm, and 935 nm transitions, respectively, are specified by the manufacturer of the wavemeter (HighFinesse/Ångstrom WS/7). The differences in the transition frequencies are measured with better precision; 60 MHz, 20 MHz, and 20 MHz are given as upper bounds of the uncertainties due to the drift of the wavemeter.

Isotope A	Transition frequency [THz]					
	369 nm transition		935 nm transition		760 nm transition	
	This work	Reference	This work	Reference	This work	Reference
168	811.29611(10)		320.562190(50)		394.432865(60)	
170	811.29439(10)	811.29440(13) [11]	320.565910(50)	320.56593(7) [11]	394.429590(60)	
172	811.29274(10)	811.29284(13) [11]	320.569390(50)	320.56941(7) [11]	394.426550(60)	394.4266[a] [7]
174	811.29146(10)	811.29154(13) [11]	320.572010(50)	320.57201(7) [11]	394.424145(60)	394.424[a] [8] 394.423900[a] [6]
176	811.29025(10)	811.29031(13) [11]	320.574515(50)	320.57449(7) [11]	394.421885(60)	

Isotope pair (A, A')	Isotope shift [MHz]		
	369 nm	935 nm	760 nm
(168,170)	1 720(60)	-3 720(20)	3 275(20)
(170,172)	1 650(60)	-3 480(20)	3 040(20)
(172,174)	1 280(60)	-2 620(20)	2 405(20)
(174,176)	1 210(60)	-2 505(20)	2 260(20)

[a] Uncertainty not specified.

TABLE S2. Masses of isotopes from Ref. [14] for the ${}^{168}\mathrm{Yb}^+$ ion, and from Refs. [15–17] for the remaining isotopes. The ionization energy of 6.254 eV for a neutral Yb atom [18, 19] is used to calculate the ion mass from the neutral-atom mass.

Isotope A	m^A [u]
168	167.93389132(10)
170	169.934767246(11)
172	171.936386659(15)
174	173.938867548(12)
176	175.942574709(16)

TABLE S3. Correlation coefficients between inverse-mass differences $\mu^{AA'}$ for different nearest-even neighboring isotope pairs.

Isotope pair (A,A')	(168,170)	(170,172)	(172,174)	(174,176)
(168,170)		-0.4430	0.1879	-0.0906
(170,172)			-0.4241	0.2045
(172,174)				-0.4822
(174,176)				

(see Table S8), which is smaller than the IS uncertainty in this work. As the precision of IS measurements increases to $O(1\,\mathrm{Hz})$ [2, 12] and further to $O(1\,\mathrm{mHz})$ [13], the atomic masses should be measured with uncertainty below $O(10^{-8}\,\mathrm{u})$ and $O(10^{-11}\,\mathrm{u})$, respectively, to avoid uncertainties in King plots being dominated by the mass uncertainties.

C. Cross-checks and improved isotope shifts

To check for systematic errors and improve our uncertainties, we perform additional redundant measurements of the IS by measuring next-next-even neighbor ISs. Then each measured quantity is a linear combination of other quantities (e.g., $\nu^{170,174} = \nu^{170,172} + \nu^{172,174}$). By combining the measured values, each of the quantities can be better estimated with a reduced uncertainty, at the slight complication of correlations between different quantities. In this work, the measured ISs for nearest-even neighboring isotope pairs $(166+2i, 166+2i+2)$, $i = 1, \cdots, 4$, and next-nearest-even neighboring isotope pairs $(166+2i, 166+2i+4)$, $i = 1, \cdots, 3$, producing improved values of the nearest-even neighboring isotope pairs' ISs from the following relation.

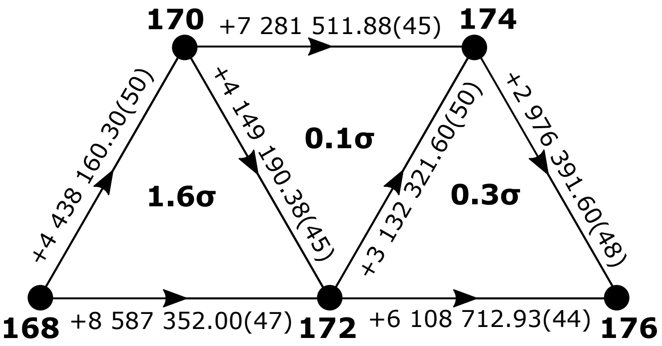

FIG. S6. Measured values of ISs (values along edges in kHz) for different pairs of Yb$^+$ isotopes (vertices labeled with the mass numbers A of isotopes ^{A}Yb$^+$) and consistency of values forming shortest loops (σ-significance in the center of each triangle). The IS value $\nu^{AA'} = \nu^A - \nu^{A'}$ is shown for an edge directed from vertex A to vertex A'. The measured values agree overall with 0.86σ significance.

$$\underbrace{\begin{bmatrix} \nu_\alpha^{168,170} \\ \nu_\alpha^{170,172} \\ \nu_\alpha^{172,174} \\ \nu_\alpha^{174,176} \\ \nu_\alpha^{168,172} \\ \nu_\alpha^{170,174} \\ \nu_\alpha^{172,176} \end{bmatrix}}_{\boldsymbol{y}} = \underbrace{\begin{bmatrix} 1 & 0 & 0 & 0 \\ 0 & 1 & 0 & 0 \\ 0 & 0 & 1 & 0 \\ 0 & 0 & 0 & 1 \\ 1 & 1 & 0 & 0 \\ 0 & 1 & 1 & 0 \\ 0 & 0 & 1 & 1 \end{bmatrix}}_{X} \underbrace{\begin{bmatrix} \nu_\alpha^{168,170} \\ \nu_\alpha^{170,172} \\ \nu_\alpha^{172,174} \\ \nu_\alpha^{174,176} \end{bmatrix}}_{\boldsymbol{\beta}} \tag{S1}$$

Finding the best estimates of the four isotope shifts $\hat{\boldsymbol{\beta}}$ from the observations $\boldsymbol{y}$ becomes a typical least square problem $\boldsymbol{y} = X\boldsymbol{\beta}$. The improved IS values $\hat{\boldsymbol{\beta}}$ are obtained via a weighted least squares fit with the weights given by inverse-squared measurement uncertainties. The values, errors, and correlations of $\hat{\boldsymbol{\beta}}$ are listed in Table S4.

The self-consistency of three measured IS values $\nu^{AA'}$, $\nu^{A'A''}$ and $\nu^{AA''}$ that involves three isotopes A, A', and A'' can be tested by, e.g., checking if the difference of $\nu^{AA'} + \nu^{A'A''}$ and $\nu^{AA''}$ is within the combined measurement uncertainty $\sqrt{(\Delta\nu^{AA'})^2 + (\Delta\nu^{A'A''})^2 + (\Delta\nu^{AA''})^2}$ (see Fig. S6). Eq. (S1) serves as a test of the self-consistency of our measurements; we find agreement of our data with the linear relation given by Eq. (S1) within 0.86σ.

D. Fitting points in King plots

Fitting our data requires a procedure that both accounts for the fact that our data points have error bars along the x axis of the King Plot (as well as along the y axis), and for the existence of correlations between the data points. These correlations arise mainly because we make redundant measurements of the isotope shifts and use them to reduce the uncertainties in the pairwise shifts. For data with uncertainties only along the y axis, correlations can be straightforwardly accounted for by using a generalized least squares (GLS) fitting procedure, which takes as an input the covariance matrix of the data. To adapt the procedure to account for errors along x, we translate the x-errors into y-errors via the slope of the fit line, and then perform an iterative GLS fit to our data.

For the two-dimensional (2D) King plot (Fig. 1 in the main text), the effect of x-errors and correlations on the fit result is not significant if the King plot is frequency-normalized (see Eq. (2) in the main text) [1]. This is is because the x-errors, when propagated to the y direction, are significantly smaller than the y-errors. This is true in general for heavy atomic species where the field shift (FS) is significantly larger than the mass shift (MS).

Table S8 compares the results of the fit with and without x-errors and correlations; we see that the two agree. This provides one of the main motivations to use the frequency-normalized King plot instead of the more conventional inverse-mass-normalized King plot, as one can easily obtain reliable fitting results via standard GLS fitting procedures, which have analytic solutions.

E. Analysis of the nonlinearity pattern

We use the following vector notation for isotope-pair-dependent parameters:

$$\boldsymbol{x} = (x^{A_1A'_1}, x^{A_2A'_2}, x^{A_3A'_3}, x^{A_4A'_4}) \tag{S2}$$

where $A_kA'_k$ are the isotopes in the k-th pair. This notation provides an alternative view of King plot: if the King plot is linear, then the vector with components $\overline{\nu}_\kappa^{AA'} = \nu_\kappa^{AA'}/\nu_\tau^{AA'}$ resides in the plane that two *King vectors* $\mathbf{1}$ and $\overline{\boldsymbol{\mu}}$ define, with $f_{\kappa\tau}$ and $K_{\kappa\tau}$ as the coefficient of the vectors, respectively.

Since the vectors are four-dimensional, one can define two vectors $\boldsymbol{\Lambda}_+$ and $\boldsymbol{\Lambda}_-$ (that we call *nonlinearity vectors*) that span the space orthogonal to the *King plane.* When measured normalized ISs $\overline{\nu}_\kappa^{AA'}$ do not exactly lie in the King plane, the out-of-plane component can be decomposed along the nonlinearity vectors with components λ_+ and λ_-. In other words, the King plane and nonlinearity plane corresponds to the best fit and the remaining residuals of the ordinary-least-square fit in the King plot, respectively. There is an infinite number of ways to define nonlinearity vectors, and we suggest the following unit vectors:

$$\begin{aligned} \boldsymbol{\Lambda}_+ &\propto (\overline{\mu}_3 - \overline{\mu}_2, \overline{\mu}_1 - \overline{\mu}_4, \overline{\mu}_4 - \overline{\mu}_1, \overline{\mu}_2 - \overline{\mu}_3) \\ \boldsymbol{\Lambda}_- &\propto (\overline{\mu}_4 - \overline{\mu}_2, \overline{\mu}_1 - \overline{\mu}_3, \overline{\mu}_2 - \overline{\mu}_4, \overline{\mu}_3 - \overline{\mu}_1) \end{aligned} \tag{S3}$$

where $\overline{\mu}_k \equiv \overline{\mu}^{A_kA'_k}$. The proposed nonlinearity vectors have several advantages: They have a fairly simple, linear

TABLE S4. Improved values and errors of ISs $\nu^{AA'} = \nu^{A} - \nu^{A'}$ between nearest-neighboring even isotope pairs (diagonal elements; in kHz) from the redundant measurements listed in Table I in the main text. Correlation coefficients between $\nu^{AA'}$ for different isotope pairs are given as off-diagonal elements.

Transition	Isotope pair (A, A')	(168,170)	(170,172)	(172,174)	(174,176)
γ: 467 nm (this work)	(168,170)	-4 438 160.85(38)	-0.4430	0.1879	-0.0906
	(170,172)		-4 149 190.66(32)	-0.4241	0.2045
	(172,174)			-3 132 321.38(33)	-0.4822
	(174,176)				-2 976 391.58(37)
α: 411 nm [1]	(168,170)	2 179 098.93(21)			
	(170,172)		2 044 854.73(30)	-0.3286	
	(172,174)			1 583 068.35(31)	
	(174,176)				1 509 055.29(28)
β: 436 nm [1]	(168,170)	2 212 391.85(37)			
	(170,172)		2 076 421.04(28)	-0.4235	
	(172,174)			1 609 181.29(20)	
	(174,176)				1 534 144.06(24)
δ: 578 nm [2]	(168,170)	1 358 484.4763(23)			
	(170,172)		1 275 772.0060(30)	-0.7546	
	(172,174)			992 714.5867(23)	
	(174,176)				946 921.7751(30)
ϵ: 361 nm [3]	(168,170)	1 781 784.73(55)	-0.2210		
	(170,172)		1 672 021.40(29)		
	(172,174)			1 294 454.41(21)	-0.3885
	(174,176)				1 233 942.14(25)

form while being orthogonal to the King vectors. This simplifies error propagation in the measured quantities $\mu^{AA'}$, $\nu_{\tau}^{AA'}$, and $\nu_{\kappa}^{AA'}$ to $\mathbf{\Lambda}_{\pm}$ and $\lambda_{\pm}$. Furthermore, the $\mathbf{\Lambda}_{+}$ and $\mathbf{\Lambda}_{-}$ vectors represent zigzag $(+-+-)$ and curved $(+--+)$ patterns of nonlinearity if $\overline{\mu}_1$ to $\overline{\mu}_4$ are in increasing order (i.e., $\overline{\mu}_k < \overline{\mu}_{k+1}$), replacing the role of $\boldsymbol{\zeta}_{\pm} = (1, -1, \pm 1, \mp 1)$ in our previous work [1].

A drawback of the above basis is that in general $\mathbf{\Lambda}_{+}$ and $\mathbf{\Lambda}_{-}$ are not orthogonal to each other. One can alternatively, for instance, keep $\mathbf{\Lambda}_{+}$ and define $\mathbf{\Lambda}_{-}$ as the vector that is orthogonal to the two King vectors and $\mathbf{\Lambda}_{+}$. With this kind of choices, however, the propagation of the uncertainty is less straightforward. Interestingly, the values of $\overline{\mu}^{AA'}$ for Yb are such that the nonlinearity vectors in Eq. (S3) are very close to being perpendicular to each other ($\mathbf{\Lambda}_{+} \cdot \mathbf{\Lambda}_{-} = 0.0014$).

The points representing the measured ISs in the $(\lambda_{+}, \lambda_{-})$ plane of expansion coefficients for the α: ${}^2S_{1/2} \to {}^2D_{5/2}$ (411 nm), β: ${}^2S_{1/2} \to {}^2D_{3/2}$ (436 nm), and γ: ${}^2F_{7/2} \to {}^2D_{3/2}$ (467 nm) transitions in Yb^{+} ions; and the δ: ${}^1S_0 \to {}^3P_0$ (578 nm), and ϵ: ${}^1S_0 \to {}^1D_2$ (361 nm) transitions in neutral Yb atoms, using $\mathbf{\Lambda}_{\pm}$ as given by Eq. (S3), for two different choices of the transition for the normalization (*reference transition*) are shown in Fig. 2 in the main text. The $\lambda_{\pm}$ plane referenced to the δ transition ($\lambda_{\pm}^{(\delta)}$) is introduced as the main graph because the ISs for the δ transition have been measured with a precision that is much higher than the other transitions, so that the uncertainties in the $\lambda_{\pm}$ values (shown as ellipses) for different transitions are not correlated to each other.

F. Three-dimensional (3D) King plot

The 3D King plot is a special case of the generalized King plot introduced in Ref. [20]. If there is one source of isotope shifts in addition to the MS and FS, denoted as $X_{\alpha} x^{AA'}$, then the isotope shift is given as

$$\nu_{\alpha}^{AA'} = K_{\alpha} \mu^{AA'} + F_{\alpha} \delta \langle r^2 \rangle^{AA'} + X_{\alpha} x^{AA'} + Y_{\alpha} y^{AA'} \tag{S4}$$

where $Y_{\alpha} y^{AA'}$ is a small fourth contribution to the IS shifts (i.e., $X_{\alpha} x^{AA'} \gg Y_{\alpha} y^{AA'}$) that we want to test for. If the ISs of three transitions ν_{α}, ν_{β}, and ν_{γ} are measured, then the unknown quantities $\delta \langle r^2 \rangle^{AA'}$ and $x^{AA'}$ can be eliminated from the expression by solving Eq. (S4) for the three transitions.

$$\begin{bmatrix}\nu_\alpha^{AA'}\\ \nu_\beta^{AA'}\\ \nu_\gamma^{AA'}\end{bmatrix}-\begin{bmatrix}Y_\alpha\\ Y_\beta\\ Y_\gamma\end{bmatrix}y^{AA'}=\underbrace{\begin{bmatrix}K_\alpha & F_\alpha & X_\alpha\\ K_\beta & F_\beta & X_\beta\\ K_\gamma & F_\gamma & X_\gamma\end{bmatrix}}_{T}\begin{bmatrix}\mu^{AA'}\\ \delta\langle r^2\rangle^{AA'}\\ x^{AA'}\end{bmatrix}\tag{S5}$$

$$\mu^{AA'}=\sum_{\chi=\alpha,\beta,\gamma}\left(T^{-1}\right)_{1\chi}\left(\nu_\chi^{AA'}-Y_\chi y^{AA'}\right)\tag{S6}$$

By rearranging Eq. (S6), we obtain the expression for inverse-mass-normalized 3D King plot as follows:

$$\overline{\overline{\nu}}_\gamma^{AA'}=K_{\gamma\beta\alpha}+f_{\gamma\beta\alpha}\overline{\overline{\nu}}_\alpha^{AA'}+f_{\gamma\alpha\beta}\overline{\overline{\nu}}_\beta^{AA'}+Y_{\gamma\beta\alpha}\overline{\overline{y}}^{AA'}\tag{S7}$$

where $\overline{\overline{z}}^{AA'}\equiv z^{AA'}/\mu^{AA'}$ ($z\in\{\nu_\alpha,\nu_\beta,\nu_\gamma,y\}$) are inverse-mass-normalized quantities [1],

$$f_{\gamma\beta\alpha}=\frac{\frac{F_\gamma}{F_\beta}-\frac{X_\gamma}{X_\beta}}{\frac{F_\alpha}{F_\beta}-\frac{X_\alpha}{X_\beta}}=\frac{X_{\gamma\beta}}{X_{\alpha\beta}}\text{ and}\tag{S8}$$

$$f_{\gamma\alpha\beta}=\frac{\frac{F_\gamma}{F_\alpha}-\frac{X_\gamma}{X_\alpha}}{\frac{F_\beta}{F_\alpha}-\frac{X_\beta}{X_\alpha}}=\frac{X_{\gamma\alpha}}{X_{\beta\alpha}}\tag{S9}$$

are the slopes of the plane in 3D the King plot along the axes corresponding to transitions α and β, respectively,

$$\begin{aligned}Z_{\gamma\beta\alpha}&=Z_\gamma-f_{\gamma\beta\alpha}Z_\alpha-f_{\gamma\alpha\beta}Z_\beta\\&=Z_{\gamma\alpha}-\frac{X_{\gamma\alpha}}{X_{\beta\alpha}}Z_{\beta\alpha}\\&=Z_{\beta\alpha}(z_{\gamma\alpha\beta}-f_{\gamma\alpha\beta})\end{aligned}\tag{S10}$$

where $Z=K,Y$ are the z-intercept of the plane and the electronic factor associated with the nonlinearity source $y^{AA'}$, respectively, and $z_{\gamma\alpha\beta}\equiv z_{\gamma\alpha}/z_{\beta\alpha}$ (see the main text for the definition of $z_{\kappa\chi}$ and $Z_{\kappa\chi}$ for $\chi\neq\kappa$). There is only one source of nonlinearity in the 2D King plot (namely $X_\alpha x^{AA'}$) if all the points in 3D King plot lie in a plane, barring the case that $\boldsymbol{y}$ can be decomposed to $\boldsymbol{\mu}$, $\boldsymbol{\delta\langle r^2\rangle}$, and $\boldsymbol{x}$ (see Sec. II E for the vector notation), or Y_α, Y_β, and Y_γ cancel out in $Y_{\gamma\beta\alpha}$. Therefore, fitting the points in the 3D King plot serves as a test if there are one or two contributions to the IS besides the MS and the FS.

We fit 3D King plots in a similar way as 2D King plots (see Sec. II D). Uncertainties and correlations in the x and y values are propagated to the z direction, and iterative GLS fits are performed.

An example 3D King plot and the linear fit are shown in Fig. S7 for the (α,γ,β) transitions.

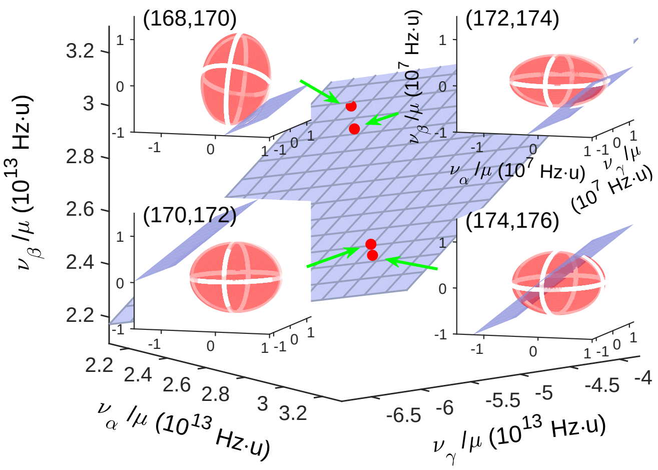

FIG. S7. Plane fitted to a 3D inverse-mass-normalized King plot constructed from isotope shifts measured on the $\alpha=411$ nm [1], $\beta=436$ nm [1] and $\gamma=467$ nm (this work) transitions for nearest-neighbor pairs of even Yb$^+$ isotopes, as described by Eq. (S7). Insets display magnified view of each point to show deviation from the fitted plane. The origin of the inset axes has been set to the center of each point. The red ellipsoids depict 1σ confidence intervals of the data. The fit to the plane gives 3.2σ significance of nonlinearity (see Table S9). Each point in the King plot is correlated with other points (see Sec. II D).

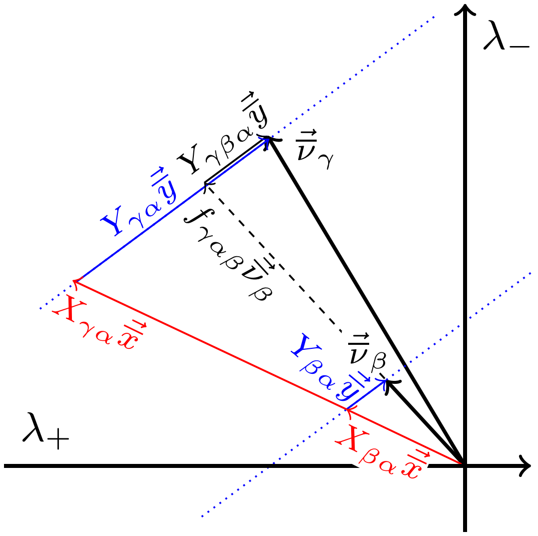

FIG. S8. Two-source-nonlinearity analysis in the (λ_+,λ_-) map with reference transition α. Thick black arrows indicate the measured ν_β and ν_γ. The nonlinearity from $x^{AA'}$ ($y^{AA'}$) is coded with red (blue) color. The blue dotted line shows the direction of $\lambda_\pm$ due to $y^{AA'}$. The 3D King plot corresponds to stretching the nonlinearity from ν_β (dashed black arrow; $f_{\gamma\beta\alpha}\overline{\overline{\boldsymbol{\nu}}}_\beta$) and moving along $y^{AA'}$'s direction (thin black arrow; $Y_{\gamma\beta\alpha}\overline{\overline{\boldsymbol{y}}}$) to form a triangle with nonlinearity for ν_γ.

1. *Equivalence between 3D King-plot linearity and single-source fit in $\lambda_\pm$ plane*

Consider a frequency-normalized 3D King plot for (α, β, γ) transitions [equivalent to Eq. (S7)]:

$$\overline{\boldsymbol{\nu}}_\gamma = K_{\gamma\beta\alpha}\overline{\boldsymbol{\mu}} + f_{\gamma\beta\alpha}\mathbf{1} + f_{\gamma\alpha\beta}\overline{\boldsymbol{\nu}}_\beta + Y_{\gamma\beta\alpha}\overline{\boldsymbol{y}} \tag{S11}$$

[see Eq. (S2) for the vector notation]. From Fig. S8, one can easily see that linear fit in 3D King plot corresponds to finding the values of $f_{\gamma\alpha\beta}$ and $Y_{\gamma\beta\alpha}$ to form a triangle along nonlinearity patterns for $\nu_\beta^{AA'}$, $\nu_\gamma^{AA'}$, and $y^{AA'}$.

Therefore, if the 3D King plot is linear, the area of the corresponding triangle vanishes. It implies $\overline{\boldsymbol{\nu}}_\beta$ and $\overline{\boldsymbol{\nu}}_\gamma$ have to be parallel to each other. Thus a test of whether two data points lie along a line through the origin in the $\lambda_\pm$ plane can be used to probe for the existence of a second nonlinearity source $y^{AA'}$ (see Fig. 2 in the main text).

It is straightforward to see that the ratio $f_{\eta\chi\kappa} = G^{(4)}_{\eta\chi}/G^{(4)}_{\kappa\chi}$ (ratio of red arrows' lengths) determines the λ_-/λ_+ ratio for $y^{AA'}$ (dotted lines in Fig. S8) and vice versa, independent of the λ_-/λ_+ ratio of the dominant source of nonlinearity $x^{AA'}$ (i.e., the direction of the red arrow). The former one is equivalent to fitting the 3D King plot with a known nonlinearity pattern from nuclear parameters $y^{AA'}$ (see Eqs. S12 and S14). The latter suggests that if $f_{\eta\chi\kappa}$ can be calculated precisely in the future, the λ_-/λ_+ ratio of the second nonlinearity source can be deduced and compared with λ_-/λ_+ from Quadratic field shift (QFS), a new boson, or any other proposed sources.

G. New-boson range

As the dominant source of nonlinearity observed in 2D King plot is expected to be from $G^{(4)}\delta\langle r^4\rangle$ (see Fig. 3 in the main text), we can eliminate the dominant source by drawing a 3D King plot. If we assume that the nonlinearity remaining in the 3D King plot is originating primarily from the new boson, we can obtain the value of $\upsilon_{ne}D_{\eta\kappa\chi}$ by fitting the King plot using the relation

$$\overline{\overline{\nu}}{}_\eta^{AA'} = K_{\eta\kappa\chi} + f_{\eta\kappa\chi}\overline{\overline{\nu}}{}_\chi^{AA'} + f_{\eta\chi\kappa}\overline{\overline{\nu}}{}_\kappa^{AA'} + \upsilon_{ne}D_{\eta\kappa\chi}\overline{\overline{a}}{}^{AA'}. \tag{S12}$$

We obtain a perfect fit as there are four fitting parameters $K_{\eta\kappa\chi}$, $f_{\eta\kappa\chi}$, $f_{\eta\chi\kappa}$, and $\upsilon_{ne}D_{\eta\kappa\chi}$ for four isotope pairs (A, A') (see Table S9). On the other hand, the calculated $D_{\eta\kappa\chi}$ at light new-boson mass m_ϕ has statistical uncertainty from the fitted value of $f_{\eta\chi\kappa}$ (see Sec. IV E). Therefore, the value of new-boson-coupling product

$$y_e y_n = (-1)^{s+1} 4\pi\hbar c \frac{(\upsilon_{ne}D_{\eta\kappa\chi})_{\text{fit}}}{(D_{\eta\kappa\chi})_{\text{cal}}} \tag{S13}$$

is given by a ratio of fitted parameter to calculated parameter. Here we use a simple way to treat uncertainties in the numerator and the denominator. We consider the 95% confidence interval of each value and conservatively obtain the range for $y_e y_n$ from the intervals.

The values of $y_e y_n$ as a function of the new-boson mass m_ϕ obtained using Eq. (S13) for some choices of (χ, κ, η) from five transitions α to ϵ are shown in Fig. 4 in the main text. There the fitted $\upsilon_{ne}D_{\eta\chi\kappa}$ have much bigger fractional uncertainties than the calculated $D_{\eta\kappa\chi}$ for the $(\chi, \kappa, \eta) = (\alpha, \gamma, \delta)$, (β, γ, δ), and $(\gamma, \delta, \epsilon)$ transitions (see Table S9), except in the regions where $D_{\eta\kappa\chi}$ is close to zero, and we have no sensitivity to a new boson for the given transition (i.e., $y_e y_n$ diverges).

H. QFS range

Similar to the new-boson bound, the experimental range of the quadratic field shift $[\delta\langle r^2\rangle^2]$ can be obtained by assuming that it is the dominant source of the observed nonlinearity in 3D King plot,

$$\overline{\overline{\nu}}{}_\eta^{AA'} = K_{\eta\kappa\chi} + f_{\eta\kappa\chi}\overline{\overline{\nu}}{}_\chi^{AA'} + f_{\eta\chi\kappa}\overline{\overline{\nu}}{}_\kappa^{AA'} + G^{(2)}_{\eta\kappa\chi}\overline{\overline{[\delta\langle r^2\rangle^2]}}{}^{AA'} \tag{S14}$$

We believe that the calculation for the (α, γ, β) transitions is the most reliable as the transitions are obtained simultaneously from a single run of the CI calculation (from GRASP2018; see Sec. IV), providing maximum consistency between the calculations for the different transitions. The fitted value of $G^{(2)}_{\beta\gamma\alpha}$ has different sign and bigger magnitude than the two-transition factor $G^{(2)}_{\beta\alpha}$ (see Tables S8 and S9). However, we expect the three-transition factor to be significantly smaller than the two-transition factor for $G^{(2)}$ (see Sec. IV E). This implies that the observed nonlinearity might not be mainly from QFS, although future measurements of the α and β transitions with the better precision might result in smaller fitted $G^{(2)}_{\beta\gamma\alpha}$.

III. ESTIMATION OF SYSTEMATIC EFFECTS AND ERRORS

Our measurement error is determined directly from the scatter of our data points. Most of the systematic effects pertaining to measurements of transition frequencies in atoms are common-mode between the isotopes, with only a small differential component that affects our measured ISs. Drifts in experimental parameters can lead to uncertainties on these differential shifts, and these are the main source of our measurement error. Many of the systematic uncertainties affecting our experiment are the same as for our previous measurement of the ISs of the quadrupole transitions [1] and are discussed in detail in the Supplemental Material of that work. While we summarize all effects in Table S5, here we discuss primarily systematic effects which differ from the previous work, due to the transition or modifications in the experimental setup.

TABLE S5. Estimated contributions to systematic shift on the γ transition. The systematic uncertainty is dominated by the laser-induced AC Stark shift.

	Estimated magnitude of absolute shift (Hz)	Estimated differential shift (Hz)
Laser-induced Stark shift	$7(1) \times 10^{3}$	$0(1) \times 10^{2}$
Linear Zeeman shift	$0(3) \times 10^{2}$	$0(3) \times 10^{2}$
Absolute frequency stability probe laser	$0(3) \times 10^{2}$	$0(3) \times 10^{2}$
Second-order Doppler shift	$5(10) \times 10^{-1}$	$2(100) \times 10^{-2}$
Micromotional Stark shift	$5(1) \times 10^{-1}$	$2(100) \times 10^{-3}$
Electric quadrupole shift	$3(3) \times 10^{-2}$	$0(3) \times 10^{-2}$
Black-body shift	$68(3) \times 10^{-3}$	$0(3) \times 10^{-3}$
Quadratic Zeeman shift	$1000(2) \times 10^{-4}$	$0(2) \times 10^{-4}$
Gravitational red shift	$100(1) \times 10^{-4}$	$0(1) \times 10^{-4}$

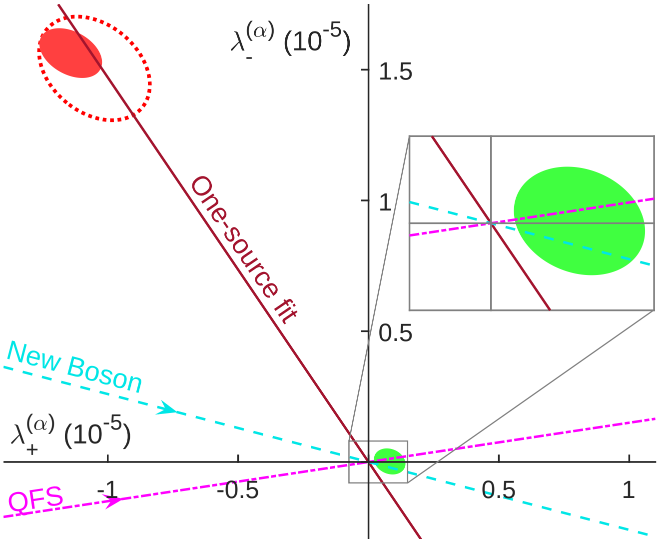

FIG. S9. (λ_+, λ_+) values of measured ISs for β (green) and γ (red) transitions normalized by ISs for α transition. See Fig. 2 in the main text for details.

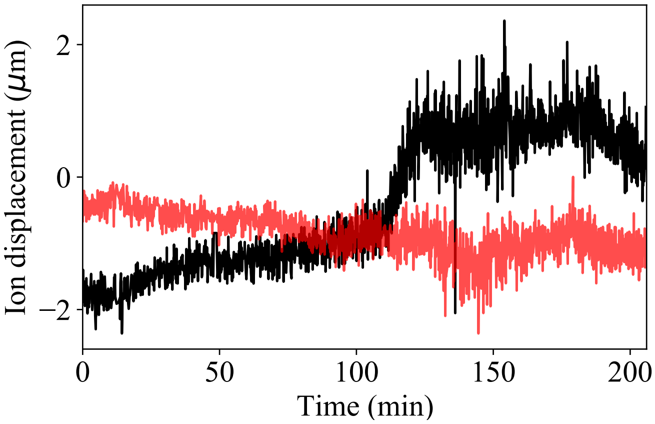

FIG. S10. Position of the ion in the plane of the trap as a function of time. The z direction is along the trap axis (black), and x is the direction perpendicular to the trap axis and parallel to the plane of the trap (red). The ion is interrogated with the same laser pulse sequence used during the experiment, but the probe laser is detuned from resonance. Decreased ion displacement along x reflects the tighter confinement along the radial trap direction.

A. AC Stark shift

The 467 nm probe light used to drive the octupole transition can also couple to other transitions in the atom, causing an intensity-dependent AC Stark shift of the transition frequency. This shift has been measured to be $5.9(8) \times 10^{-5}\,\mathrm{Hz\,W^{-1}\,m^{2}}$ [12]. For our beam waist, power and polarization, this leads to a shift of ∼7 kHz. The shift is common-mode between different isotopes but can introduce an error in the IS measurement if there is a systematic variation of the probe laser intensity when tuned to different isotope transition frequencies or due to random fluctuations in intensity between isotopes which do not completely average out over our measurements. We stabilize the power of the probe beam such that power fluctuations at a monitor photodiode are kept below 0.5%, corresponding to an error of 35 Hz. We also note, however, that our UV laser beams can periodically charge the trap chip, shifting the minimum of the trapping potential and moving the ion relative to the center of the beam. Any such effect could lead to changes in the effective intensity seen by the ion. To determine the size of this effect, we monitored the ion fluorescence on a camera and tracked the ion's position while subjecting it to the sequence of laser pulses used in the experiment. We observed a drift $\lesssim 2$ μm in the ion position in the plane of the trap (see Fig. S10), indicating that the ion could experience intensity fluctuations of around 1%, giving an error of order 100 Hz. We note, however, that our camera monitoring of the ion position has no sensitivity to drifts perpendicular to the plane of the trap. It is possible that drifts in this direction are a contributing source of the ~ 2 kHz spread we observe in the data [see Fig. S5(a) for an example dataset].

B. Absolute frequency stability of probe laser

The frequency stability of our probe laser is currently limited by a residual amplitude modulation (RAM) of the PDH error signal used to lock the laser to a resonance of the ULE cavity.

1. *RAM stabilization*

RAM originating from the fiber EOM has the potential to introduce noise in the PDH frequency stabilization. Following Ref. [21], we employ a RAM stabilization scheme feeding back to the DC voltage input of the fiber EOM and the temperature control of the EOM crystal. Deviating from the scheme employed in Ref. [21], we feed the DC voltage signal into the temperature control servo.

To obtain a measure of the RAM remaining in our system, we continuously monitored the off-resonant PDH error signal. With our stabilization system engaged, we found that the effect of RAM was suppressed to a level below our measurement resolution, bounding its contribution to the probe laser frequency instability to ≤ 300 Hz.

2. *ULE-cavity transmission power stabilization*

Light at infrared wavelengths is used to lock the Ti:Sapphire laser to the ULE cavity. Drifts in the power of the intracavity light can change the heating in the mirror coatings, and systematically shift the ULE cavity frequency. To counter this effect, we stabilize the power transmitted through the cavity with an AOM.

To quantify the effect of intracavity power fluctuations on the probe laser frequency, we performed a spectroscopy experiment on the 467 nm transition of $^{174}\mathrm{Yb}^+$. The cavity transmission power was varied between two values ($29\,\mu$W and $42\,\mu$W). For each value of power, we took two transition frequency scans, then switched to the other power. Each transition scan takes ~ 8 minutes, so that the total duration of the experiment was 5 hours. We plot the results in Fig. S11 and determine that the reference frequency drifts $-1.11(85)$ kHz for $13\,\mu$W increase in optical power (i.e., $-85(65)$ Hz/μW).

Residual frequency drifts in the probe laser can originate from variations in the set point of the servo loop for the cavity transmission power, at $24\,\mu$W. Assuming temperature variations in the laboratory of $\pm 2°$C, the drift in the control electronics can introduce a maximum error of 25 Hz.

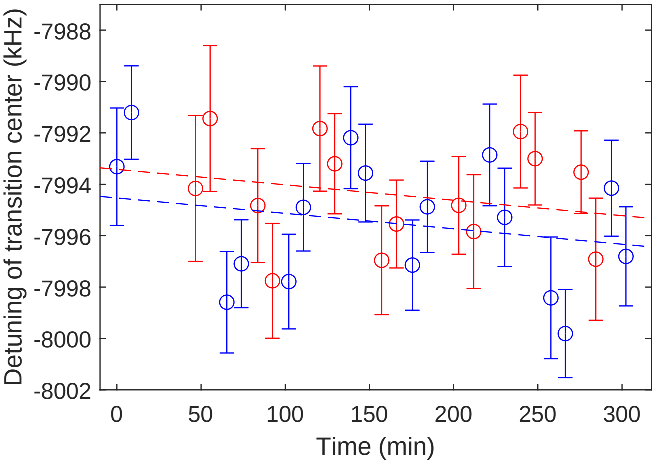

FIG. S11. Measured transition center frequency plotted against time for two different values of the ULE cavity transmission power. Blue and red data points correspond to $42\,\mu W$ and $29\,\mu W$ of transmitted power, respectively. An offset was subtracted from the vertical axis, which is not shown here. The linear fit corresponds to the common drift of the reference cavity. The fitted frequency shift is 1.11(85) kHz.

C. Linear Zeeman shift

In order to minimize the uncertainty on the measurement of the transition frequency introduced by drifts in the magnetic field between scans, we perform interleaved scans of transitions B and R (the two transitions we measure to determine the center, which are symmetrically blue and red detuned from the center) – i.e. we measure one point on the scan of the red transition, then one point on the scan of the blue transition, then the next point on the red transition and so on. The time needed to measure a point on a given transition and switch to measuring the other transition is of order 10 s.

We can extract an estimate for our magnetic-field noise by evaluating the differential drift of the measured resonant frequencies of the B and R transitions. We find that the RMS differential drift to be of order 5 kHz, which implies a magnetic-field noise on the order of 3 mG. This level of noise is expected due to a local subway station and is consistent with what we measure in other experiments. We find no significant correlation between this measure of magnetic field and the measured centers of the transitions, indicating that it is unlikely that our magnetic-field noise is contributing systematic shifts to our measurement.

D. Black-body shift

The black-body radiation shifts on the transition are well approximated by [22]

$$\Delta\nu_{\mathrm{BBR}} = -\frac{1}{2}\Delta\alpha_0(831.9\,\mathrm{V\,m^{-1}})^2\left(\frac{T}{300\,\mathrm{K}}\right)^4 \qquad \text{(S15)}$$

where $\Delta\alpha_0$ is the difference in scalar polarizability between the atomic states associated with the transition of interest, measured to be $-1.3(6) \times 10^{-40}\,\mathrm{J\,V^{-2}\,m^2}$ [5]. This gives a shift of 68 mHz at 300 K. We conservatively estimate that the temperature of the chamber can drift by 3 K during a measurement, yielding a change in $\Delta\nu_{\mathrm{BBR}} \sim 3\,\mathrm{mHz}$.

E. Electric quadrupole shift

A frequency shift results from the interaction of the electric quadrupole moment of the two states with electric field gradients from the trap. The shift is of order

$$\Delta\nu_{\mathrm{quad}} \sim \frac{\Theta \cdot \nabla E}{h}. \tag{S16}$$

The quadrupole moment of the ${}^2F_{7/2}$ state has been measured at $-0.041(5)\,ea_0^2$ [5]. Time-varying electric field gradients due to patch potentials on the chip trap can lead to a differential shift between isotopes. We observe a typical day-to-day variation of the DC micromotion compensation voltages applied to our trap electrodes of 20 mV. Conservatively, we consider a maximum variation of 200 mV during the course of a shift measurement data-taking run. From this, we infer that differential patch-potential gradients of order $\sim 1\,\mathrm{V\,mm^{-2}}$ could occur, which would lead to a differential quadrupole shift of $\sim 30\,\mathrm{mHz}$.

F. Second-order Doppler shift and Stark shift due to micromotion

Both the second-order Doppler shift and the Stark shift due to micromotion contribute systematic uncertainties that are several orders of magnitude below the leading systematics on our experiment. For completeness, we update our estimate of these systematics here employing the same calculation described in the Supplemental Material of Ref. [1]. To estimate the stray DC fields and micromotion amplitudes experienced by the ion, we use our measurement of the maximum excursion made by the ion from the trap center over the course of a day while exposed to the sequence of laser pulses used in the experiment (as described in Sec. III A, we expect that our tightly focused probe laser beam and UV Doppler cooling beams may cause charging of the trap chip, leading to drifts in the ion position). We estimate a contribution to our error budget on the order of 1 Hz from the second-order Doppler shift and 0.1 Hz from the Stark shift.

G. Frequency pulling of the measured transition center due to imperfect centering of the scan range

As shown in Fig. S3, the 760 nm repumper light is turned off during the readout stage of our laser pulse sequence. This introduces a small probability of a false quantum jump reading due to rare events where the probe transition has not been successfully driven but the ion still falls into the $F_{7/2}$ state through other channels (according to Ref. [23]; this likely occurs due to collisions with background gas and happens once every few hours). Because we determine the center of a frequency scan by taking the statistical mean of the points, if our scan range is not perfectly centered on the transition resonance frequency, this effect could slightly pull our transition center frequency. However, if we instead find the center by fitting the transition lineshape, we should be insensitive to this effect (since it would, on average, contribute a background that is symmetric around the transition center). To bound this potential error source (and any other potential pulling of the line due to imperfect centering of our scan range), we compare the results of our analysis with one where we fit the datapoints to a Gaussian function with background offset. We find that there is no difference between the two methods within our statistical error bars.

IV. ATOMIC STRUCTURE CALCULATIONS AND ELECTRONIC FACTORS

Atomic-structure calculations (ASCs) are performed using Dirac-Hartree-Fock (DHF) [24, 25] and subsequent configuration interaction (CI) methods [26–29] using two different calculation packages available: GRASP2018 [1, 30] and AMBiT [31, 32].

A. Calculations using GRASP2018

We use the popular package GRASP2018 [30] to solve for the electronic wavefunction associated with each atomic state. We perform two calculations with GRASP2018: one for the ${}^1S_0$ and ${}^3P_0$ states in neutral Yb for the 576 nm clock transition, and another for the ${}^1S_{1/2}$, ${}^2D_{3/2}$, ${}^2D_{5/2}$, and ${}^2F_{7/2}$ states in singly-ionized Yb for the 435, 411, and 467 nm clock transitions. In both calculations we use multi-configuration DHF calculations; first we obtain radial wavefunctions for orbitals in the ^{172}Yb core (up to $5s^2 5p^6 4f^{14}$) followed by the valence orbitals ($6s$, $6p$, and $5d$). Then, we construct a basis for correlation orbitals. Finally, we perform a configuration interaction (CI) calculation to obtain mixing coefficients for the different configuration state functions (CSFs) in the expansion.

For neutral Yb, correlation orbitals up to $10spdfg$ are constructed in the Thomas-Fermi approximation. To construct the CSFs for the ${}^1S_0$ and ${}^3P_0$ states, we begin with a multireference consisting of the $4f^{14}6s^2$, $4f^{14}6s6p$, $4f^{13}6s^2 5d$, and $4f^{14}6s5d$ configurations. We allow for a single excitation originating from any of the valence orbitals or select core orbitals ($4spd$ and $5sp$); we find this produces sufficient agreement with experimentally-measured clock transition wavelengths.

For the Yb$^+$ ion, correlation orbitals up to $8spdf$ are calculated via DHF. For $^2S_{1/2}$, $^2D_{5/2}$, $^2D_{3/2}$, and $^2F_{7/2}$ states, single and double excitations from $6s$, $6p$, and $5d$ shells and single excitations from $4f$ shell are allowed in $4f^{14}6s$, $4f^{14}6p$, $4f^{14}5d$, $4f^{13}6s^2$, $4f^{13}6s5d$, $4f^{13}6p^2$, and $4f^{13}5d^2$ to generate the CSFs. Single excitations from $4sp$ and $5sp$ core shells are also allowed for $4f^{14}6s$, $4f^{14}6p$, and $4f^{13}6s^2$ configurations. The total number of excitations is limited to two.

From the calculated wavefunction for a state specified by its total angular momentum J and parity P, the radial electron density $\rho(r)$[1] can be obtained from the expression $\rho(r) = \langle\Psi|\sum_{i=1}^{N}\delta(r-|\mathbf{r}_i|)|\Psi\rangle$ where $\Psi = \sum_\nu c_\nu\Phi(\gamma_\nu PJM_J)$ is the atomic state function with CSFs $\Phi(\gamma_\nu PJM_J)$ and associated mixing coefficients c_ν, $\delta(r-|\mathbf{r}_i|)$ are one-dimensional Dirac-delta functions for i-th electron's position $\mathbf{r}_i$, and $N = Z - I$ is the number of electrons in an (ionized) atom [33]. REDF1, a program for extracting radial electron densities from GRASP2018 calculation results has been developed by modifying and merging the source codes for RHFS routine in GRASP2018 and RIS4 routine [33] since our previous work [1]. The routine is available in Ref. [34]. Finally, the change in the electron density during the χ transition is given as $\rho_\chi(r) = \rho_\chi^{(e)}(r) - \rho_\chi^{(g)}(r)$ where $\rho_\chi^{(g)}(r)$ and $\rho_\chi^{(e)}(r)$ are the densities for the ground and excited states, respectively.

B. Calculations using AMBiT

The particle-hole CI calculations using AMBiT [35] are performed in the closed-core DHF potential (V^{N-1} for Yb$^+$). The valence $6s$, $6p$, and $5d$ DHF orbitals are generated in this potential. Higher orbitals nlj are constructed by multiplying the upper component of the $(n-1)lj$ orbital by the simple radial function r, and orthogonalizing with the lower orbitals [36]. The lower component is constructed from the upper component using the Dirac equation. The $5f$ orbital is specially created by multiplying the $5d$ orbital by r and orthogonalizing to $4f$.

For Yb$^+$, the CI calculation includes orbitals up to $8spdf$. Configurations were then generated by allowing single and double-electron excitations from the valence orbitals in the leading configurations $6s$, $5d$, $6p$, $4f^{-1}\ 6s^2$, $4f^{-1}\ 5d\ 6s$, $4f^{-1}\ 5d^2$, and $4f^{-1}\ 6p^2$. One additional excitation from the $4f$ shell was also allowed. In this way we captured most of the important configurations. CSFs were then created for each total angular momentum and parity J^π.

The calculation for neutral Yb was very similar. The basis was extended to $12spdf$ and single and double-electron excitations were generated from the leading configurations $6s^2$, $6s\ 6p$, $6p^2$, and $6s\ 5d$, with additional single excitations from the $5s$ and $5p$ orbitals.

C. Single-transition electronic factors

Single-transition electronic factors can be derived from the wavefunctions or transition frequencies calculated via ASCs. From the GRASP2018 output REDF1 routine, the change in electron density over space $\rho_\chi(\boldsymbol{r})$ during the transition χ can be extracted, and the procedures to obtain single-transition electronic factors F_χ, K_χ, $G_\chi^{(4)}$, and D_χ are elaborated in the Supplement Material of our previous paper [1]. We have changed the strategy to obtain $G_\chi^{(2)}$ to avoid numerical noise from repeated ASCs pointed out in Ref. [37]. It is assumed that the finite size of the nucleus caps the electronic wavefunction which would diverge at the origin if the nucleus were a point charge. This gives the relation

$$\rho_\chi(0;\langle r^2\rangle) = C_\chi\rho_\chi^P(r^2 = \langle r^2\rangle) \tag{S17}$$

where $\rho_\chi(0)$[2] is the change in electronic density at the origin with the finite nuclear size $\langle r^2\rangle$ during the transition χ, ρ_χ^P is the density for point-charge nucleus, and C_χ is a constant for the size of the nucleus. Then $G_\chi^{(2)}$ is given as

$$\begin{aligned} G_\chi^{(2)} &= \frac{1}{2}\frac{\partial^2\nu_\chi}{(\partial\langle r^2\rangle)^2}(\langle r^2\rangle^A) = \frac{1}{2}\frac{\partial F_\chi}{\partial\langle r^2\rangle}(\langle r^2\rangle^A) \\ &= \frac{c\alpha' Z}{96\pi^2}\frac{\partial\rho_\chi(0;\langle r^2\rangle)}{\partial\langle r^2\rangle}(\langle r^2\rangle^A) \\ &= C_\chi\frac{c\alpha' Z}{96\pi^2}\frac{\partial\rho_\chi^P}{\partial r^2}(\langle r^2\rangle^A) \end{aligned} \tag{S18}$$

where c is the speed of light, $\alpha' \approx 1/137$ is the fine structure constant, and $Z = 70$ is the proton number of Yb, for a reference isotope A (here we choose $A = 172$). Therefore, a single atomic structure calculation with a point-charge nucleus is sufficient to obtain $G_\chi^{(2)}$. It is numerically observed that $C_\alpha = 1.04$, essentially unity, for transition α: $^2S_{1/2} \to {}^2D_{1/2}$ (411 nm) transition. A similar idea appears in Ref. [38] for the analytic estimation of the King plot nonlinearity.

For AMBiT, The ASCs are repeated for transition χ while varying nuclear parameters $z = \mu, \delta\langle r^2\rangle, a$, and the rates of the change in transition frequency $(\partial\nu_\chi)/(\partial z)$ are taken as the associated electronic factors K_χ, F_χ, and

---

[1] It is the one-dimensional density and normalized as follows: $\int \mathrm{d}r\rho(r) = N$.

[2] Here the electron density function is three-dimensional (i.e., $\int \mathrm{d}\boldsymbol{r}\rho^{(e,g)}(\boldsymbol{r}) =$ (the number of electrons) for ground or excited states in a given transition).

D_χ, respectively. $G^{(2)}_\chi$ is given as the second derivative $\frac{1}{2}(\partial^2\nu_\chi)/(\partial\delta\langle r^2\rangle)^2$. For K_χ, the nuclear inverse mass μ is promoted to a finite field parameter by adding a relativistic mass shift operator to the Coulomb interaction [39].

The values of the single-transition electronic factors for the five transitions α to ϵ in this paper are tabulated in Table S7 and shown in Fig. S14.

D. Two-transition electronic factors

Two-transition electronic factors $f_{\kappa\chi} = F_\kappa/F_\chi$ and $Z_{\kappa\chi} = Z_\kappa - f_{\kappa\chi}Z_\chi$ where $Z \in \{K, G^{(4)}, G^{(2)}, D\}$ are defined for (2D) King plots (see the main text), and are calculated from the single-transition factors from ASCs.

The values of the two-transition electronic factors for all possible transition pairs out of the five transitions α to ϵ can be found in Table S8 and Fig. S15.

E. Three-transition electronic factors

Three-transition electronic factors $f_{\eta\chi\kappa} = G^{(4)}_{\eta\chi}/G^{(4)}_{\kappa\chi}$ and $Z_{\eta\kappa\chi} = Z_{\eta\chi} - f_{\eta\chi\kappa}Z_{\kappa\chi}$ where $Z \in \{K, G^{(2)}, D\}$ are defined for the 3D King plot (see Sec. II F), assuming that the fourth-moment field shifts $G^{(4)}_{\chi,\kappa,\eta}\delta\langle r^4\rangle_{ji}$ are the dominant source of the nonlinearity in 2D King plot (see Fig. 2 in the main text). Their values are calculated from the two-transition factors.

We have the choice of using the calculated or the fitted $f_{\eta\chi\kappa}$ to obtain $Z_{\eta\kappa\chi} = Z_{\kappa\chi}(z_{\eta\chi\kappa} - f_{\eta\chi\kappa})$. Unfortunately, the calculated and fitted values of $f_{\eta\chi\kappa}$ are significantly different for the current accuracy of our ASCs (see Table S9). For the electronic factors Z that are expected to have a strong correlation to $G^{(4)}$ (i.e., $z_{\eta\chi\kappa} - f_{\eta\chi\kappa} \ll 1$) such as $G^{(2)}$ and D at heavy new-boson mass $m_\phi \gtrsim 10^7\,\text{eV}$ (corresponds to the nuclear size), using the calculated $f_{\eta\chi\kappa}$ would be better to ensure $z_{\eta\chi\kappa} - f_{\eta\chi\kappa} \ll 1$ and obtain the right order of magnitude (see Fig. S12). The strong correlation is because all of the factors probe the properties of electronic wavefunction near the origin. For K and D at the lighter mass $m_\phi \lesssim 10^4\,\text{eV}$ (corresponds to the Bohr radius), the correlation with $G^{(4)}$ is not expected in general as they encode the global shape of the wavefunction. Therefore, we determine that using experimental value of $f_{\eta\chi\kappa}$ is the better choice.

Note that the situation for two-transition factors is similar, $Z_{\kappa\chi} = Z_\chi(z_{\kappa\chi} - f_{\kappa\chi})$, and here the calculated $f_{\kappa\chi}$ are used for all Z as they agree sufficiently well with the fitted values (see Table S8).

The values of the electronic factors for all possible choices of three transitions out of the five transitions α to ϵ are listed in Table S9, and plotted in Fig. S16.

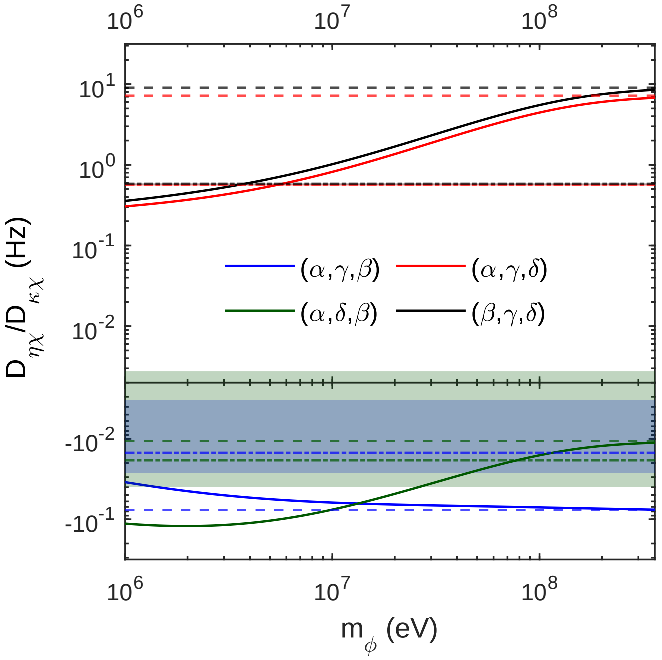

FIG. S12. $d_{\eta\chi\kappa} = D_{\eta\chi}/D_{\kappa\chi}$ ratio derived from atomic structure calculations (ASCs) performed using GRASP2018 [30] vs new boson mass m_ϕ for various transitions (χ, κ, η) (solid line) coded with different colors (see legend). Dashed lines indicate corresponding $f_{\eta\chi\kappa} = G^{(4)}_{\eta\chi}/G^{(4)}_{\kappa\chi}$ ratios derived from the ASCs. Dash-dotted lines and shaded area show $f_{\eta\chi\kappa}$ and their 1σ uncertainties obtained from linear fit in the corresponding 3D King plots. (The shaded regions are not visible for (α, γ, δ) and (β, γ, δ) transitions as the areas are too thin.) Theoretical and experimental values of $f_{\eta\chi\kappa}$ can be found in Table S9.

F. Estimating mass shift coefficient K_κ from reliable K_χ calculation and $K_{\kappa\alpha}$ from measured ISs

It is challenging to calculate mass shift coefficients K_χ for heavy atoms precisely [40, 41]. This turns out to be especially the case for the γ: ${}^2S_{1/2} \rightarrow {}^2F_{7/2}$ (467 nm) transition; values from calculations with GRASP2018 and AMBiT don't agree on the sign, and neither of them predicts $K_{\gamma\alpha}$ close enough the experimental value from the King plot (see Tables S7 and S8, and Fig. 3(d) in the main text). On the other hand, the calculated mass shift coefficient for the α: ${}^2S_{1/2} \rightarrow {}^2D_{5/2}$ (411 nm) transition and the β: ${}^2S_{1/2} \rightarrow {}^2D_{3/2}$ (436 nm) transition are relatively reliable; values from GRASP2018 and AMBiT agree to about factor of two, and the experimental value of $K_{\beta\alpha}$ agrees relatively well with the values from GRASP2018 and AMBiT. This is presumably because the α and β transitions have relatively simpler electronic configurations, in which a valence electron is excited to higher orbitals while the core configuration is maintained, while the γ transition corresponds to the excitation of a core electron from the $4f$ shell to $6s$ valence orbital. In a case like this, where the value of K_χ is more reliable than K_κ, we can relate them via the experimentally accurately measured quantities $K_{\kappa\chi}$ and $f_{\kappa\chi}$,

$$K_\kappa = K_{\kappa\chi} + f_{\kappa\chi} K_\chi, \tag{S19}$$

which serves as a benchmark for the calculated K_κ (See Fig. 3(d) in the main text).

V. NUCLEAR CALCULATIONS AND NUCLEAR CHARGE MOMENTS

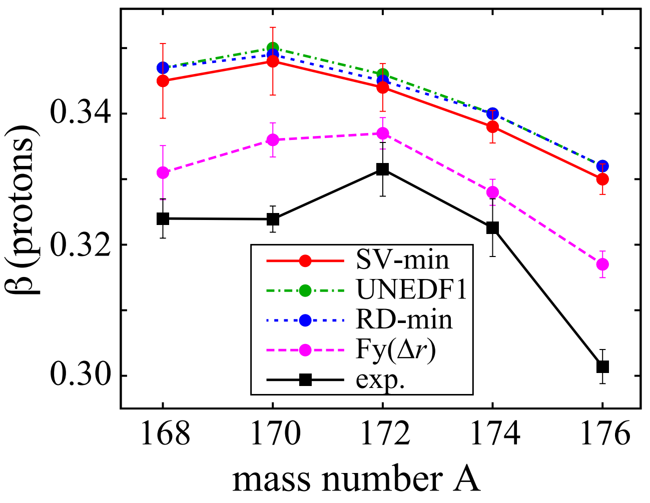

FIG. S13. Quadrupole ground-state deformations β for ^{168,170,172,174,176}Yb obtained in nuclear DFT with different EDFs compared to empirical values [42].

A. Radii from nuclear mean-field models

For the theoretical description of nuclear charge densities, we use here self-consistent mean-field models at the level of nuclear DFT [43]. In particular, we employ the energy density functionals (EDFs) SV-min [44], RD-min [45], UNDEF1 [46], and Fy(Δr) [47]. SV-min and UNEDF1 are based on the standard Skyrme functional [43]. RD-min replaces the power-law density dependence of the Skymre functional by a rational approximant. Fy(Δr) uses the Fayans functional which has additionally gradient terms in pairing and surface energy. The model parameters of all four EDFs are calibrated to a large set of nuclear ground state data. SV-min, RD-min, and Fy(Δr) use a large set of data from spherical nuclei and information from the electromagnetic form factor [44]. In addition Fy(Δr) has also been optimized to differential charge radii of Ca isotopes [47]. The large dataset of UNEDF1 employs energies and charge radii of spherical and deformed nuclei. In all variants, we use the density-dependent pairing force treated in the BCS approximation. With these four EDFs we explore different functional forms as well as different optimization strategies. This should give an impression on these various influences, see the discussion of theoretical results in the main text.

Another crucial aspect is the post-processing of the emerging proton and neutron density distributions to obtain a reliable charge density. This requires proper inclusion of the nucleons charge distribution, relativistic corrections, especially magnetic spin-orbit correction, which must be included in precision calculations of radial moments. Our DFT calculations take all these effects into account (see, e.g., Figs. 4, 6, and 7 of Ref. [48]). As there is no choice in that respect, all four EDFs are processed with that strategy.

The considered Yb isotopes are all significantly deformed. Thus we use a DFT solver employing an axially symmetric grid in coordinate space which allows for reflection-symmetric deformations [49]. The radial charge moments $\langle r^n\rangle$ are directly obtained from the calculated nuclear charge distribution $\rho_n(\boldsymbol{r})$ (See Table S6). Figure S13 shows dimensionless ground-state quadrupole proton deformations β obtained in our DFT calculations and compares them to the empirical values [42]. The deformations are defined in the usual way: $\beta = 4\pi Q_{20}/(3ZR_0^2)$, where Q_{20} is the proton quadrupole moment and $R_0 = 1.2\,\mathrm{fm}\,A^{1/3}$. It is satisfactory to see that the calculations are consistent with experiment, considering the scale of β. In particular the maximum of β is predicted by Fy(Δr) at $A = 172$ in agreement with the experiment.

B. Nonlinearity pattern from calculated $\delta\langle r^4\rangle$

Caution is necessary when calculating nonlinearity patterns from higher-order charge moments $\delta\langle r^n\rangle$ ($n > 2$) from nuclear calculations. $\delta\langle r^n\rangle$ and $\delta\langle r^2\rangle$ are obtained from difference in nuclear charge distributions $\delta\rho_n^{AA'}(r)$ between isotopes A and A' given by a nuclear calculation, and thus highly correlated to each other. Since the FS, which is proportional to $\delta\langle r^2\rangle$, is the dominant source of total IS, *calculated* ISs using $\delta\langle r^2\rangle$ from nuclear calculation should be used to ensure self-consistency as follows. It is especially important when the calculated $\delta\langle r^2\rangle$ do not reflect actual experimentally determined pattern (see Fig. 3(a) in the main text), as then the position of the points in King plot will be different, which changes the nonlinearity pattern significantly.

$G^{(4)}_{\gamma\alpha}\overline{\delta\langle r^4\rangle}^{AA'}_{\perp}$, the nonlinearity from $\delta\langle r^4\rangle^{AA'}$, is given as the component of the vector

$$\begin{aligned} G^{(4)}_{\gamma\alpha}\overline{\delta\langle r^4\rangle}^{AA'} &= G^{(4)}_{\gamma\alpha}\frac{\delta\langle r^4\rangle^{AA'}}{\nu_\alpha^{AA'}} \\ &= \frac{G^{(4)}_{\gamma\alpha}}{F_\alpha}\frac{\delta\langle r^4\rangle^{AA'}}{\delta\langle r^2\rangle^{AA'} + \frac{K_\alpha}{F_\alpha}\mu^{AA'} + \frac{G^{(4)}_\alpha}{F_\alpha}\delta\langle r^4\rangle^{AA'}} \end{aligned} \tag{S20}$$

TABLE S6. Upper table: Theoretical and experimental values of difference in nuclear charge moments $\delta\langle r^2\rangle$ and $\delta\langle r^4\rangle$ between isotopes. The values for nuclear DFT calculations using SV-min, RD-min, UNEDF1, and Fy(Δr) EDFs are listed in columns 2 – 5 and 8 – 11. Columns 6 and 7 tabulate the values of $\delta\langle r^2\rangle$ from measured ISs in α transition and calculated F_α and K_α for GRASP2018 [30] and AMBiT [31], respectively (see Table S7). Lower table: Theoretical values of $\langle r^2\rangle^A$, $\langle r^4\rangle^A$, and quadrupole deformation β^A. For β^A, we show also the experimental values derived from the measured B(E2) values [42]; see also Fig. S13.

Isotope pair (A, A')	$\delta\langle r^2\rangle^{AA'}$ [fm^2]						$\delta\langle r^4\rangle^{AA'}$ [fm^4]			
	Nuclear DFT				Measured ν_α		Nuclear DFT			
	SV-min	RD-min	UNEDF1	Fy(Δr)	GRASP	AMBiT	SV-min	RD-min	UNEDF1	Fy(Δr)
(168, 170)	−0.159(23)	−0.159(43)	−0.175	−0.203	−0.145	−0.154	−10.6(2.1)	−10.6(3.8)	−11.8	−14.3
(170, 172)	−0.125(29)	−0.128(65)	−0.139	−0.169	−0.136	−0.145	−7.4(3.1)	−7.6(6.7)	−8.3	−11.4
(172, 174)	−0.119(48)	−0.127(100)	−0.135	−0.120	−0.107	−0.113	−6.8(4.8)	−7.4(10.)	−8.1	−6.8
(174, 176)	−0.126(32)	−0.134(50)	−0.134	−0.134	−0.102	−0.108	−7.2(3.7)	−7.8(5.2)	−8.0	−7.2

Isotope	$\langle r^2\rangle^A$ [fm^2]				$\langle r^4\rangle^A$ [fm^4]				β^A				
A	SV-min	RD-min	UNEDF1	Fy(Δr)	SV-min	RD-min	UNEDF1	Fy(Δr)	SV-min	RD-min	UNEDF1	Fy(Δr)	Exp.
168	27.769	27.776	27.939	27.494	1012.9	1012.5	1021.4	991.03	0.345	0.347	0.347	0.331	0.324
170	27.927	27.935	28.113	27.697	1023.5	1023.1	1033.2	1005.4	0.348	0.349	0.350	0.336	0.324
172	28.052	28.064	28.252	27.866	1030.9	1030.7	1041.5	1016.8	0.344	0.345	0.346	0.337	0.332
174	28.171	28.190	28.388	27.986	1037.6	1038.1	1049.6	1023.6	0.338	0.340	0.340	0.328	0.323
176	28.297	28.325	28.522	28.120	1044.8	1045.9	1057.6	1030.8	0.330	0.332	0.332	0.317	0.301

which is orthogonal to **1** and

$$\overline{\mu}^{AA'} \propto \frac{\mu^{AA'}}{\delta\langle r^2\rangle^{AA'} + \frac{K_\alpha}{F_\alpha}\mu^{AA'} + \frac{G_\alpha^{(4)}}{F_\alpha}\delta\langle r^4\rangle^{AA'}} \tag{S21}$$

(see Sec. II E for the vector notation). One can see that the nonlinearity arises mainly from the difference in $\delta\langle r^2\rangle^{AA'}$ and $\delta\langle r^4\rangle^{AA'}$'s patterns up to an overall scale, and it is thus important to use not only $\delta\langle r^4\rangle^{AA'}$ from nuclear calculations, but also the IS calculated using $\delta\langle r^2\rangle^{AA'}$ from the same nuclear calculation for self-consistency. We have numerically verified that using measured values of $\nu_\alpha^{AA'}$ to normalize $\mu^{AA'}$ and $\delta\langle r^2\rangle^{AA'}$ results in a significantly different $\lambda_-/\lambda+$ ratio from the observed nonlinearity. The change in the ratio K_α/F_α and $G_\alpha^{(4)}/F_\alpha$ can tune the values of $\overline{\mu}^{AA'}$, $\overline{\delta\langle r^4\rangle}^{AA'}$, and thus the nonlinearity $\lambda_\pm$.

The largest inset in Fig. 2 in the main text shows the nonlinearity $\lambda_\pm$ predicted by the nuclear DFT calculations. The solid lines across the symbols show the change in $\lambda_\pm$ when $G_\alpha^{(4)}/F_\alpha$ ratio changes by ±50% of the calculated value. Changing K_α in between -2604.4 GHz·u and +174.2 GHz·u, which covers three times the difference in K_α values for the GRASP2018 and AMBiT calculations, moves $\lambda_\pm$ points along the solid lines by smaller amounts.

Calculations for all of the four nuclear DFTs predict a λ_-/λ_+ ratio fairly close to the measured ISs, despite the significant difference in the measured and calculated $\delta\langle r^2\rangle$. In particular, the Fy(Δr) functional predicts the λ_-/λ_+ ratio consistent with the measured ISs to within 2σ. It also predicts a reasonable magnitude of $\lambda_\pm$ when the results are combined with the calculated $G_{\gamma\alpha}^{(4)}/F_\alpha$ (see Tables S7 and S8). Note that the Fy(Δr) is also the only functional that predicts qualitatively correctly $\delta\langle r^2\rangle$ ratios out of the four functionals used in this work (see Fig. 3(a) in the main text), as well as the deformation parameter β (Fig. S13). The effect of uncertainly in the calculated $G_{\gamma\alpha}^{(4)}/F_\alpha$ ratio is a mere scaling of the distance in $\lambda_\pm$ plane from the origin along the λ_-/λ_+ ratio line. Interestingly, it is numerically observed that the effects of change in the K_α/F_α or $G_\alpha^{(4)}/F_\alpha$ ratios are similar to the change in $G_{\gamma\alpha}^{(4)}/F_\alpha$ ratio [i.e., the change of nonlinearity in (λ_+, λ_-) plane is almost purely radial from the origin]. This suggests that the calculated λ_-/λ_+ ratios are robust with respect to the uncertainty in the calculated electronic factors.

---

[1] I. Counts, J. Hur, D. P. L. Aude Craik, H. Jeon, C. Leung, J. C. Berengut, A. Geddes, A. Kawasaki, W. Jhe, and V. Vuletić, Evidence for nonlinear isotope shift in Yb$^+$ search for new boson, Phys. Rev. Lett. **125**, 123002 (2020).

[2] K. Ono, Y. Saito, T. Ishiyama, T. Higomoto, T. Takano,

Y. Takasu, Y. Yamamoto, M. Tanaka, and Y. Takahashi, Observation of non-linearity of generalized King plot in the search for new boson, arXiv:2110.13544 [Phys. Rev. X].

[3] N. L. Figueroa, J. C. Berengut, V. A. Dzuba, V. V. Flambaum, D. Budker, and D. Antypas, Precision determination of isotope shifts in ytterbium and implications for new physics, Phys. Rev. Lett. **128**, 073001 (2022).

[4] P. Taylor, M. Roberts, S. V. Gateva-Kostova, R. B. M. Clarke, G. P. Barwood, W. R. C. Rowley, and P. Gill, Investigation of the $^2S_{1/2}$–$^2D_{5/2}$ clock transition in a single ytterbium ion, Phys. Rev. A **56**, 2699 (1997).

[5] N. Huntemann, M. Okhapkin, B. Lipphardt, S. Weyers, C. Tamm, and E. Peik, High-accuracy optical clock based on the octupole transition in ^{171}Yb$^+$, Phys. Rev. Lett. **108**, 090801 (2012).

[6] A. M. Ransford, *Old Dog, New Trick: High Fidelity, Background-free State Detection of an Ytterbium Ion Qubit*, Ph.D. thesis, The University of California, Los Angeles (2020).

[7] Y.-Y. Jau, J. D. Hunker, and P. D. D. Schwindt, F-state quenching with CH4 for buffer-gas cooled ^{171}Yb$^+$ frequency standard, AIP Adv. **5**, 117209 (2015).

[8] K. Sugiyama, A. Wakita, and A. Nakata, Diode-laser-based light sources for laser cooling of trapped Yb$^+$ ions, in *Conference on Precision Electromagnetic Measurements. Conference Digest. CPEM 2000* (Cat. No.00CH37031) (IEEE, Sydney, 2000) pp. 509–510, 10.1109/CPEM.2000.851105.

[9] S. Mulholland, H. A. Klein, G. P. Barwood, S. Donnellan, P. B. R. Nisbet-Jones, G. Huang, G. Walsh, P. E. G. Baird, and P. Gill, Compact laser system for a laser-cooled ytterbium ion microwave frequency standard, Rev. Sci. Instrum. **90**, 033105 (2019).

[10] C. L. Edmunds, T. R. Tan, A. R. Milne, A. Singh, M. J. Biercuk, and C. Hempel, Scalable hyperfine qubit state detection via electron shelving in the $^2D_{5/2}$ and $^2F_{7/2}$ manifolds in ^{171}Yb$^+$, Phys. Rev. A **104**, 012606 (2021).

[11] J. J. McLoughlin, A. H. Nizamani, J. D. Siverns, R. C. Sterling, M. D. Hughes, B. Lekitsch, B. Stein, S. Weidt, and W. K. Hensinger, Versatile ytterbium ion trap experiment for operation of scalable ion-trap chips with motional heating and transition-frequency measurements, Phys. Rev. A **83**, 013406 (2011).

[12] H. A. Fürst, C.-H. Yeh, D. Kalincev, A. P. Kulosa, L. S. Dreissen, R. Lange, E. Benkler, N. Huntemann, E. Peik, and T. E. Mehlstäubler, Coherent excitation of the highly forbidden electric octupole transition in ^{172}Yb$^+$, Phys. Rev. Lett. **125**, 163001 (2020); Erratum, Phys. Rev. Lett. **128**, 149901(E) (2022).

[13] T. Manovitz, R. Shaniv, Y. Shapira, R. Ozeri, and N. Akerman, Precision measurement of atomic isotope shifts using a two-isotope entangled state, Phys. Rev. Lett. **123**, 203001 (2019).

[14] D. Nesterenko, R. de Groote, T. Eronen, Z. Ge, M. Hukkanen, A. Jokinen, and A. Kankainen, High-precision mass measurement of ^{168}Yb for verification of nonlinear isotope shift, Int. J. Mass Spectrom. **458**, 116435 (2020).

[15] W. Huang, G. Audi, M. Wang, F. G. Kondev, S. Naimi, and X. Xu, The AME2016 atomic mass evaluation (I). Evaluation of input data; and adjustment procedures, Chin. Phys. C **41**, 030002 (2017).

[16] M. Wang, G. Audi, F. G. Kondev, W. Huang, S. Naimi, and X. Xu, The AME2016 atomic mass evaluation (II). Tables, graphs and references, Chin. Phys. C **41**, 030003 (2017).

[17] R. Rana, M. Höcker, and E. G. Myers, Atomic masses of strontium and ytterbium, Phys. Rev. A **86**, 050502(R) (2012).

[18] A. Kramida, Y. Ralchenko, and J. Reader (NIST ASD Team), NIST Atomic Spectra Database (ver. 5.9), [Online]. Available: `https://physics.nist.gov/asd` (2021, November 2). National Institute of Standards and Technology, Gaithersburg, MD (2021).

[19] M. Aymar, A. Debarre, and O. Robaux, Highly excited levels of neutral ytterbium. II. Multichannel quantum defect analysis of odd- and even-parity spectra, J. Phys. B **13**, 1089 (1980).

[20] K. Mikami, M. Tanaka, and Y. Yamamoto, Probing new intra-atomic force with isotope shifts, Eur. Phys. J. C **77**, 896 (2017).

[21] W. Zhang, M. J. Martin, C. Benko, J. L. Hall, J. Ye, C. Hagemann, T. Legero, U. Sterr, F. Riehle, G. D. Cole, and M. Aspelmeyer, Reduction of residual amplitude modulation to 1×10^{-6} for frequency modulation and laser stabilization, Opt. Lett. **39**, 1980 (2014).

[22] M. S. Safronova, M. G. Kozlov, and C. W. Clark, Blackbody radiation shifts in optical atomic clocks, IEEE Trans. Ultrason. Ferroelectr. Freq. Control **59**, 439 (2012).

[23] S. Olmschenk, K. C. Younge, D. L. Moehring, D. N. Matsukevich, P. Maunz, and C. Monroe, Manipulation and detection of a trapped Yb$^+$ hyperfine qubit, Phys. Rev. A **76**, 052314 (2007).

[24] I. Grant, B. McKenzie, P. Norrington, D. Mayers, and N. Pyper, An atomic multiconfigurational Dirac-Fock package, Comput. Phys. Commun. **21**, 207 (1980).

[25] K. Dyall, I. Grant, C. Johnson, F. Parpia, and E. Plummer, GRASP: A general-purpose relativistic atomic structure program, Comput. Phys. Commun. **55**, 425 (1989).

[26] P. Jönsson, A. Ynnerman, C. Froese Fischer, M. R. Godefroid, and J. Olsen, Large-scale multiconfiguration Hartree-Fock and configuration-interaction calculations of the transition probability and hyperfine structures in the sodium resonance transition, Phys. Rev. A **53**, 4021 (1996).

[27] S. G. Porsev, M. G. Kozlov, and D. Reimers, Transition frequency shifts with fine-structure constant variation for Fe I and isotope-shift calculations in Fe I and Fe II, Phys. Rev. A **79**, 032519 (2009).

[28] B. Fawcett and M. Wilson, Computed oscillator strengths, Landé g values, and lifetimes in Yb II, At. Data Nucl. Data Tables **47**, 241 (1991).

[29] E. Biémont, J.-F. Dutrieux, I. Martin, and P. Quinet, Lifetime calculations in Yb II, J. Phys. B **31**, 3321 (1998).

[30] C. Froese Fischer, G. Gaigalas, P. Jönsson, and J. Bieroń, GRASP2018 - a Fortran 95 version of the general relativistic atomic structure package, Comput. Phys. Commun. **237**, 184 (2019).

[31] E. Kahl and J. Berengut, AMBiT: A programme for high-precision relativistic atomic structure calculations, Comput. Phys. Commun. **238**, 232 (2019).

[32] J. C. Berengut, C. Delaunay, A. Geddes, and Y. Soreq, Generalized King linearity and new physics searches with isotope shifts, Phys. Rev. Research **2**, 043444 (2020).

[33] J. Ekman, P. Jönsson, M. Godefroid, C. Nazé, G. Gaigalas, and J. Bieroń, RIS4: A program for relativistic isotope shift calculations, Comput. Phys. Commun. **235**, 433 (2019).

[34] J. Hur, REDF (v1.0.0), Zenodo, 10.5281/zenodo.5818081 (2022).

[35] J. C. Berengut, D. Budker, C. Delaunay, V. V. Flambaum, C. Frugiuele, E. Fuchs, C. Grojean, R. Harnik, R. Ozeri, G. Perez, and Y. Soreq, Probing new long-range interactions by isotope shift spectroscopy, Phys. Rev. Lett. **120**, 091801 (2018).

[36] P. Bogdanovich and G. Žukauskas, Approximate allowance for superposition of configurations in atomic spectra, Sov. Phys. Collect. **23**, 13 (1983).

[37] S. O. Allehabi, V. A. Dzuba, V. V. Flambaum, and A. V. Afanasjev, Nuclear deformation as a source of the nonlinearity of the King plot in the Yb^+ ion, Phys. Rev. A **103**, L030801 (2021).

[38] V. V. Flambaum, A. J. Geddes, and A. V. Viatkina, Isotope shift, nonlinearity of King plots, and the search for new particles, Phys. Rev. A **97**, 032510 (2018).

[39] J. C. Berengut, V. A. Dzuba, and V. V. Flambaum, Isotope-shift calculations for atoms with one valence electron, Phys. Rev. A **68**, 022502 (2003).

[40] A. Papoulia, B. G. Carlsson, and J. Ekman, Effect of realistic nuclear charge distributions on isotope shifts and progress towards the extraction of higher-order nuclear radial moments, Phys. Rev. A **94**, 042502 (2016).

[41] M. Puchalski and K. Pachucki, Nuclear structure effects in the isotope shift with halo nuclei, Hyperfine Interact. **196**, 35 (2010).

[42] B. Pritychenko, M. Birch, B. Singh, and M. Horoi, Tables of E2 transition probabilities from the first 2+ states in even–even nuclei, At. Data Nucl. Data Tables **107**, 1 (2016).

[43] M. Bender, P.-H. Heenen, and P.-G. Reinhard, Self-consistent mean-field models for nuclear structure, Rev. Mod. Phys. **75**, 121 (2003).

[44] P. Klüpfel, P.-G. Reinhard, T. J. Bürvenich, and J. A. Maruhn, Variations on a theme by Skyrme: A systematic study of adjustments of model parameters, Phys. Rev. C **79**, 034310 (2009).

[45] J. Erler, P. Klüpfel, and P.-G. Reinhard, Exploration of a modified density dependence in the Skyrme functional, Phys. Rev. C **82**, 044307 (2010).

[46] M. Kortelainen, J. McDonnell, W. Nazarewicz, P.-G. Reinhard, J. Sarich, N. Schunck, M. V. Stoitsov, and S. M. Wild, Nuclear energy density optimization: Large deformations, Phys. Rev. C **85**, 024304 (2012).

[47] P.-G. Reinhard and W. Nazarewicz, Toward a global description of nuclear charge radii: Exploring the Fayans energy density functional, Phys. Rev. C **95**, 064328 (2017).

[48] P.-G. Reinhard and W. Nazarewicz, Nuclear charge densities in spherical and deformed nuclei: Toward precise calculations of charge radii, Phys. Rev. C **103**, 054310 (2021).

[49] P.-G. Reinhard, B. Schuetrumpf, and J. Maruhn, The axial Hartree–Fock + BCS code SkyAx, Comput. Phys. Commun. **258**, 107603 (2021).

[50] M. Roberts, P. Taylor, S. V. Gateva-Kostova, R. B. M. Clarke, W. R. C. Rowley, and P. Gill, Measurement of the $^2S_{1/2}$–$^2D_{5/2}$ clock transition in a single $^{171}\text{Yb}^+$ ion, Phys. Rev. A **60**, 2867 (1999).

[51] C. Tamm, S. Weyers, B. Lipphardt, and E. Peik, Stray-field-induced quadrupole shift and absolute frequency of the 688-THz $^{171}\text{Yb}^+$ single-ion optical frequency standard, Phys. Rev. A **80**, 043403 (2009).

[52] S. Webster, R. Godun, S. King, G. Huang, B. Walton, V. Tsatourian, H. Margolis, S. Lea, and P. Gill, Frequency measurement of the $^2\text{S}_{1/2}$–$^2\text{D}_{3/2}$ electric quadrupole transition in a single $^{171}\text{Yb}^+$ ion, IEEE Trans. Ultrason. Ferroelectr. Freq. Control **57**, 592 (2010).

[53] S. A. King, R. M. Godun, S. A. Webster, H. S. Margolis, L. A. M. Johnson, K. Szymaniec, P. E. G. Baird, and P. Gill, Absolute frequency measurement of the $^2S_{1/2}$–$^2F_{7/2}$ electric octupole transition in a single ion of $^{171}\text{Yb}^+$ with 10^{-15} fractional uncertainty, New J. Phys. **14**, 013045 (2012).

[54] M. Pizzocaro, F. Bregolin, P. Barbieri, B. Rauf, F. Levi, and D. Calonico, Absolute frequency measurement of the $^1S_0$–$^3P_0$ transition of ^{171}Yb with a link to international atomic time, Metrologia **57**, 035007 (2020).

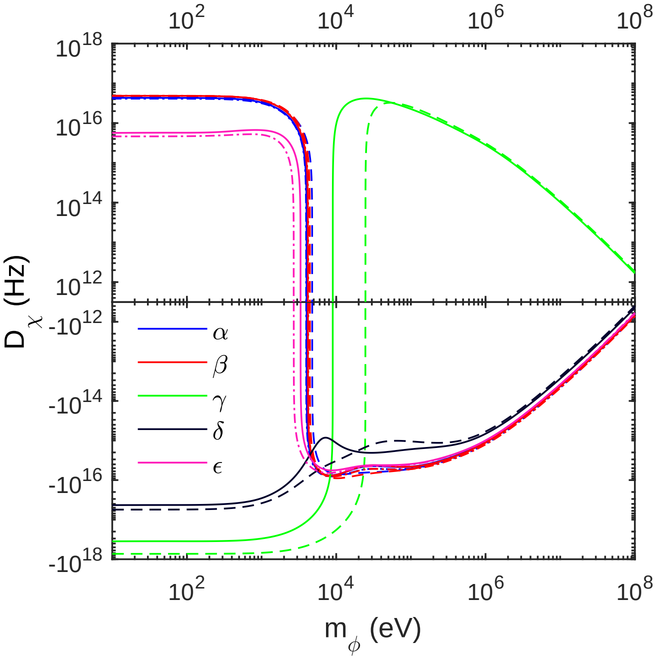

FIG. S14. Single-transition factors D_χ vs new-boson mass m_ϕ for five transitions χ coded with different colors (see legend) derived from atomic structure calculations using CI method. Solid, dashed, and dash-dotted lines are for AMBiT, GRASP2018, and Ref. [3], respectively.

TABLE S7. Calculated and experimental values of single-transition electronic factors Z_χ ($Z \in \{F, K, G^{(4)}, G^{(2)}, D\}$) for $\chi = \alpha$: ${}^2S_{1/2} \to {}^2D_{5/2}$ (411 nm), β: ${}^2S_{1/2} \to {}^2D_{3/2}$ (436 nm), and γ: ${}^2S_{1/2} \to {}^2F_{7/2}$ (467 nm) transitions in Yb$^+$ ions; and δ: ${}^1S_0 \to {}^3P_0$ (578 nm), and ϵ: ${}^1S_0 \to {}^1D_2$ (361 nm) transitions in neutral Yb atoms. $\omega_\chi/(2\pi)$ are transition frequencies. Other quantities are defined in the main text. Calculated values for each transition are obtained from CI method using GRASP2018 or AMBiT (see Sec. IV). The units of $\omega_\chi/(2\pi)$, F_χ, K_χ, $G_\chi^{(4)}$, $G_\chi^{(2)}$, and D_χ are THz, GHz/fm^2, GHz·u, MHz/fm^4, MHz/fm^4, and 10^3 THz, respectively.

	GRASP	AMBiT	Ref. [3]	Exp.
$\omega_\alpha/(2\pi)$	808.11	707.00		729.47[a] [b]
$\omega_\beta/(2\pi)$	770.13	679.86		688.36[a] [c]
$\omega_\gamma/(2\pi)$	580.12	1051.44		642.12[a] [d]
$\omega_\delta/(2\pi)$	458.36	522.78		518.30[a] [e]
$\omega_\epsilon/(2\pi)$		819.47		829.76[a] [f]
F_α	-15.852	-14.715	-17.604	
F_β	-16.094	-14.968	-18.003	
F_γ	41.892	36.218		
F_δ	-9.1508	-9.719		
F_ϵ		-13.528	-14.437	
K_α	-1678.2	-752		
K_β	-1638.5	-661		
K_γ	3127.6	12001		
K_δ				
K_ϵ				
$G_\alpha^{(4)}$	14.934		13.08	
$G_\beta^{(4)}$	15.159		13.37	
$G_\gamma^{(4)}$	-39.422			
$G_\delta^{(4)}$	8.951			
$G_\epsilon^{(4)}$			10.42	
$G_\alpha^{(2)}$	42.565	81.908	28.53	
$G_\beta^{(2)}$	43.204	83.247	28.53	
$G_\gamma^{(2)}$	-112.33	-201.12		
$G_\delta^{(2)}$		54.277		
$G_\epsilon^{(2)}$		75.322	23.34	
D_α[g]	44.145	43.158	41.235	
D_β[g]	48.419	48.634	48.795	
D_γ[g]	-730.4	-352.38		
D_δ[g]	-55.729	-42.855		
D_ϵ[g]		5.6683	4.6238	

[a] The exact value varies by the few-GHz isotope shifts.
[b] Ref. [4, 50]
[c] Ref. [51, 52]
[d] Ref. [5, 12, 53]
[e] Ref. [54]
[f] Ref. [18]
[g] At $m_\phi = 1$ eV. Values over different m_ϕ's are shown in Fig. S14

TABLE S8: Calculated and experimental values of two-transition electronic factors $f_{\kappa\chi}$ and $Z_{\kappa\chi}$ ($Z \in \{K, G^{(4)}, G^{(2)}, D\}$) for $\chi, \kappa \in \{\alpha, \beta, \gamma, \delta, \epsilon\}$. The values are calculated from the single-transition values in Table S7. $f_{\chi\kappa}$ is dimensionless. The units of $K_{\kappa\chi}$, $G^{(4)}_{\kappa\chi}$, $G^{(2)}_{\kappa\chi}$, and $D_{\kappa\chi}$ are GHz·u, kHz/fm^4, kHz/fm^4, and 10^3 THz, respectively. The last two columns ("Fit") are for data from linear fit of corresponding 2D King plots $\overline{\nu}_{\kappa}^{AA'} = f_{\kappa\chi} + K_{\kappa\chi}\overline{\mu}^{AA'}$ with ("X corr.") and without ("No X corr.") uncertainties in and correlations between independent variables (see Sec. II D). $\chi^2_{\kappa\chi}$ and $s_{\kappa\chi}$ are χ^2 and the significance of linear fit, respectively.

	GRASP	AMBiT	Ref. [3]	Fit	
				X corr.	No X corr.
$f_{\beta\alpha}$	1.0152	1.0172	1.0227	1.01141025(86)	1.01141025(86)
$f_{\gamma\alpha}$	-2.6427	-2.4613		-2.2213082(14)	-2.2213084(13)
$f_{\delta\alpha}$	0.57727	0.66048		0.61172988(34)	0.61172995(35)
$f_{\epsilon\alpha}$		0.91933	0.8201	0.81761175(80)	0.81761175(80)
$f_{\gamma\beta}$	-2.603	-2.4197		-2.1962536(14)	-2.1962537(13)
$f_{\delta\beta}$	0.5686	0.64932		0.60482313(37)	0.60482322(37)
$f_{\epsilon\beta}$		0.90379	0.80192	0.80838924(76)	0.80838924(76)
$f_{\delta\gamma}$	-0.21844	-0.26835		-0.275391225(69)	-0.275391430(78)
$f_{\epsilon\gamma}$		-0.37352		-0.36807660(27)	-0.36807657(28)
$f_{\epsilon\delta}$		1.3919		1.33656619(92)	1.33656619(92)
$K_{\beta\alpha}$	65.306	103.92		120.208(23)	120.208(23)
$K_{\gamma\alpha}$	-1307.6	10150		5737.593(39)	5737.595(35)
$K_{\delta\alpha}$				363.1350(94)	363.1332(97)
$K_{\epsilon\alpha}$				1.811(21)	1.811(21)
$K_{\gamma\beta}$	-1137.6	10402		6001.679(38)	6001.683(35)
$K_{\delta\beta}$				290.5263(97)	290.5242(99)
$K_{\epsilon\beta}$				-95.402(20)	-95.402(20)
$K_{\delta\gamma}$				1943.2126(37)	1943.2019(43)
$K_{\epsilon\gamma}$				2113.679(14)	2113.681(14)
$K_{\epsilon\delta}$				-483.666(15)	-483.666(15)
$G^{(4)}_{\beta\alpha}$	-3.5056		-6.4622		
$G^{(4)}_{\gamma\alpha}$	45.789				
$G^{(4)}_{\delta\alpha}$	329.81				
$G^{(4)}_{\epsilon\alpha}$			-306.88		
$G^{(4)}_{\gamma\beta}$	36.664				
$G^{(4)}_{\delta\beta}$	331.8				
$G^{(4)}_{\epsilon\beta}$			-301.7		
$G^{(4)}_{\delta\gamma}$	339.81				
$G^{(4)}_{\epsilon\gamma}$					
$G^{(4)}_{\epsilon\delta}$					

Continued on the next page

TABLE S8 (continued)

	GRASP	AMBiT	Ref. [3]	Fit	
				X Corr.	No X corr.
$G^{(2)}_{\beta\alpha}$	-10.442	-68.645	-646.64		
$G^{(2)}_{\gamma\alpha}$	162.69	471.33			
$G^{(2)}_{\delta\alpha}$		181.24			
$G^{(2)}_{\epsilon\alpha}$		22.9	-57.388		
$G^{(2)}_{\gamma\beta}$	135.51	305.24			
$G^{(2)}_{\delta\beta}$		225.81			
$G^{(2)}_{\epsilon\beta}$		84.94	461.17		
$G^{(2)}_{\delta\gamma}$		307.72			
$G^{(2)}_{\epsilon\gamma}$		198.95			
$G^{(2)}_{\epsilon\delta}$		-229.38			
$D_{\beta\alpha}$[a]	3.6016	4.7337	6.6257		
$D_{\gamma\alpha}$[a]	-613.74	-246.15			
$D_{\delta\alpha}$[a]	-81.212	-71.359			
$D_{\epsilon\alpha}$[a]		-34.008	-29.464		
$D_{\gamma\beta}$[a]	-604.37	-234.7			
$D_{\delta\beta}$[a]	-83.26	-74.433			
$D_{\epsilon\beta}$[a]		-38.286	-34.82		
$D_{\delta\gamma}$[a]	-215.28	-137.41			
$D_{\epsilon\gamma}$[a]		-125.95			
$D_{\epsilon\delta}$[a]		65.321			
$\chi^2_{\beta\alpha}$				11.792	11.738
$\chi^2_{\gamma\alpha}$				1755.2	2057
$\chi^2_{\delta\alpha}$				10504	10010
$\chi^2_{\epsilon\alpha}$				74.581	74.575
$\chi^2_{\gamma\beta}$				2220.6	2546
$\chi^2_{\delta\beta}$				16555	15916
$\chi^2_{\epsilon\beta}$				137.48	137.91
$\chi^2_{\delta\gamma}$				57854	43986
$\chi^2_{\epsilon\gamma}$				2040.2	1920.7
$\chi^2_{\epsilon\delta}$				4511.9	4512
$s_{\beta\alpha}$				2.99σ	2.99σ
$s_{\gamma\alpha}$				41.8σ	45.3σ
$s_{\delta\alpha}$				102σ	100σ
$s_{\epsilon\alpha}$				8.36σ	8.36σ
$s_{\gamma\beta}$				47σ	50.4σ
$s_{\delta\beta}$				129σ	126σ
$s_{\epsilon\beta}$				11.5σ	11.5σ
$s_{\delta\gamma}$				241σ	210σ
$s_{\epsilon\gamma}$				45.1σ	43.7σ
$s_{\epsilon\delta}$				67.1σ	67.1σ

[a] At $m_\phi = 1$ eV. Values over different m_ϕ's are shown in Fig. S15

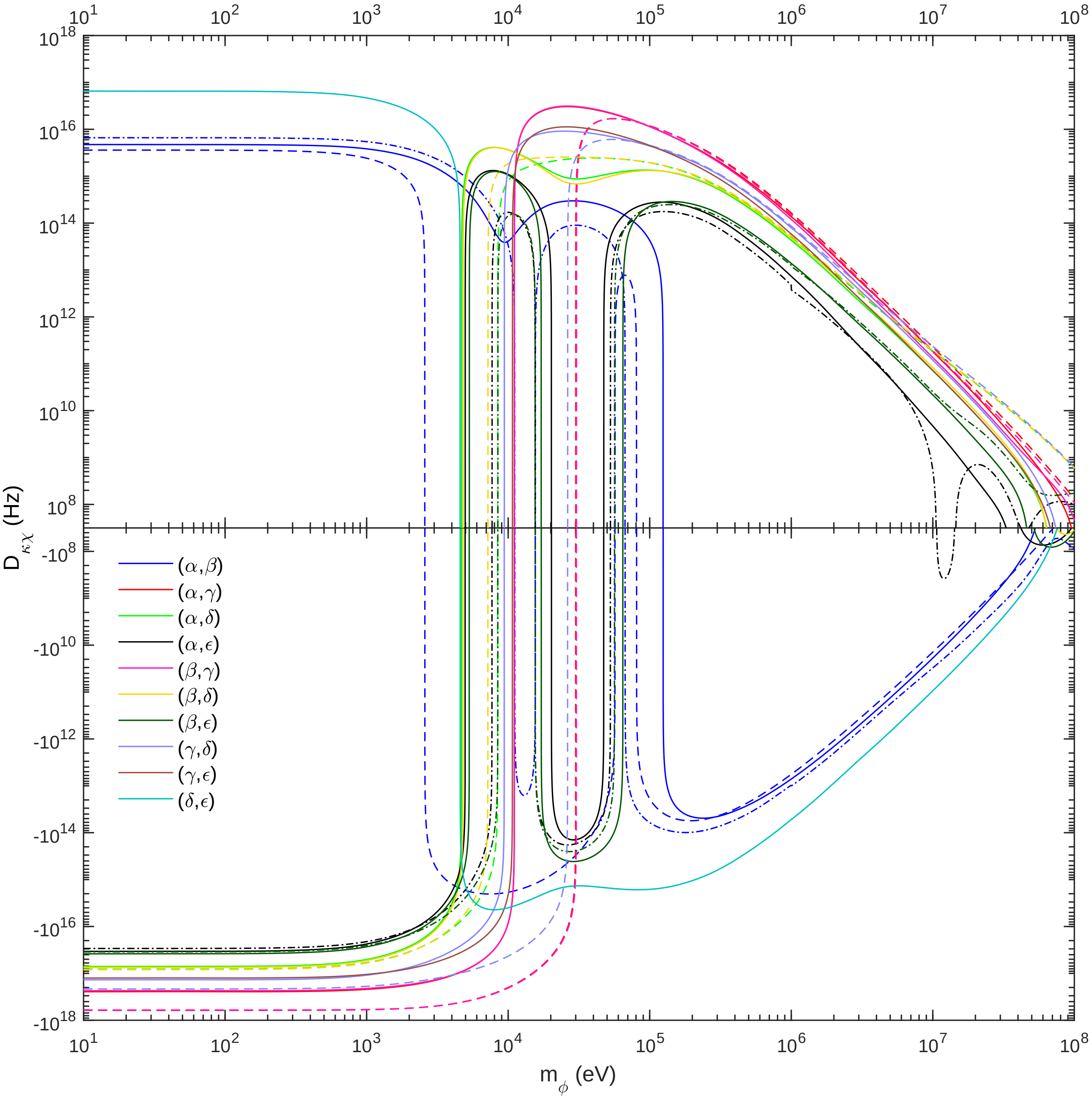

FIG. S15. Two-transition factors $D_{\kappa\chi}$ vs new-boson mass m_ϕ for variable transition pairs (χ,κ) coded with different colors (see legend) calculated using D_χ and D_κ in Fig. S14. Solid, dashed, and dash-dotted lines are for AMBiT, GRASP2018, and Ref. [3], respectively (some of dashed and dash-dotted lines are missing as the corresponding $D_{\kappa\chi}$ are not available; see Table S8).

TABLE S9: Calculated and experimental values of three-transition electronic factors $f_{\eta\kappa\chi}$ and $Z_{\eta\kappa\chi}$ ($Z \in \{K, G^{(2)}, D\}$) for $\chi, \kappa, \eta \in \{\alpha, \beta, \gamma, \delta, \epsilon\}$. The quantities are defined in Sec. II F. The values are calculated from the two-transition values in Table S8. $f_{\eta\kappa\chi}$ is dimensionless. The units of $K_{\eta\kappa\chi}$, $G^{(2)}_{\eta\kappa\chi}$, $D_{\eta\kappa\chi}$, and $\upsilon_{ne}D_{\chi\kappa}$ are GHz·u, kHz/fm^4, kHz/fm^4, 10^3 THz, and kHz, respectively. The last three columns (“Fit”) are for data from fit of corresponding 3D King plots $\overline{\overline{\nu}}_{\eta}^{AA'} = K_{\eta\kappa\chi} + f_{\eta\kappa\chi}\overline{\overline{\nu}}_{\chi}^{AA'} + f_{\eta\chi\kappa}\overline{\overline{\nu}}_{\kappa}^{AA'}$ (“Linear“), and $G^{(2)}_{\eta\kappa\chi}\overline{\overline{[\delta\langle r^2\rangle^2]}}^{AA'}$ (“QFS”) or $\upsilon_{ne}D_{\eta\kappa\chi}\overline{\overline{a}}^{AA'}$ (“New boson”) terms in addition to the relation. $\chi^2_{\eta\kappa\chi}$ and $s_{\eta\kappa\chi}$ are χ^2 and the significance of fit, respectively.

	GRASP		AMBiT		Ref. [3]		Fit		
	Cal.	Exp.	Cal.	Exp.	Cal.	Exp.	Linear	QFS	New boson
$f_{\beta\gamma\alpha}$	0.81292						0.978(26)	0.998(27)	1.052(36)
$f_{\beta\delta\alpha}$	1.0214						1.023(13)	1.018(13)	0.993(16)
$f_{\beta\epsilon\alpha}$					1.0054		1.14(10)	1.058(99)	0.86(12)
$f_{\delta\gamma\alpha}$	19.612						1.867(41)	1.877(41)	1.965(51)
$f_{\epsilon\gamma\alpha}$							1.049(30)	1.046(33)	1.040(45)
$f_{\epsilon\delta\alpha}$							0.701(13)	0.707(14)	0.717(19)
$f_{\delta\gamma\beta}$	24.126						1.885(35)	1.880(37)	1.868(49)
$f_{\epsilon\gamma\beta}$							1.090(28)	1.047(31)	0.989(43)
$f_{\epsilon\delta\beta}$							0.673(11)	0.695(13)	0.722(19)
$f_{\epsilon\delta\gamma}$							-0.2082(32)	-0.2146(38)	-0.2223(54)
$f_{\beta\alpha\gamma}$	-0.076559						-0.015(12)	-0.006(12)	0.018(16)
$f_{\beta\alpha\delta}$	-0.010629						-0.019(21)	-0.010(21)	0.030(26)
$f_{\beta\alpha\epsilon}$					0.021058		-0.15(12)	-0.06(12)	0.18(15)
$f_{\delta\alpha\gamma}$	7.2027						0.565(18)	0.570(19)	0.609(23)
$f_{\epsilon\alpha\gamma}$							0.104(14)	0.103(15)	0.100(20)
$f_{\epsilon\alpha\delta}$							0.191(21)	0.180(23)	0.165(31)
$f_{\delta\beta\gamma}$	9.0498						0.583(16)	0.580(17)	0.575(22)
$f_{\epsilon\beta\gamma}$							0.128(13)	0.109(14)	0.082(20)
$f_{\epsilon\beta\delta}$							0.223(19)	0.187(22)	0.143(32)
$f_{\epsilon\gamma\delta}$							0.580(12)	0.557(14)	0.529(20)
$K_{\beta\gamma\alpha}$	-34.804	89(21)		-80(160)			206(66)	154(69)	17(91)
$K_{\beta\delta\alpha}$							126.9(7.7)	124.2(7.8)	111.1(9.0)
$K_{\beta\epsilon\alpha}$							120.48(23)	120.53(21)	121.79(43)
$K_{\delta\gamma\alpha}$							-2880(110)	-2900(110)	-3130(130)
$K_{\epsilon\gamma\alpha}$							-596(79)	-587(85)	-570(120)
$K_{\epsilon\delta\alpha}$							-67.6(7.6)	-63.8(8.3)	-59(11)
$K_{\delta\gamma\beta}$							-3207(97)	-3190(100)	-3160(130)
$K_{\epsilon\gamma\beta}$							-865(77)	-749(86)	-590(120)
$K_{\epsilon\delta\beta}$							-160.3(5.5)	-150.1(6.4)	-138.8(8.8)
$K_{\epsilon\delta\gamma}$							986(23)	1031(27)	1083(38)

Continued on the next page

TABLE S9 (continued)

	GRASP		AMBiT		Ref. [3]			Fit	
	Cal.	Exp.	Cal.	Exp.	Cal.	Exp.	Linear	QFS	New boson
$G^{(2)}_{\beta\gamma\alpha}$	2.0139	-13.4(2.6)		-77.3(7.5)				57(18)	
$G^{(2)}_{\beta\delta\alpha}$				-74.1(4.6)				58(18)	
$G^{(2)}_{\beta\epsilon\alpha}$				-72.8(3.4)	-645.43	-636.1(8.6)		57(18)	
$G^{(2)}_{\delta\gamma\alpha}$				-106(11)				94(24)	
$G^{(2)}_{\epsilon\gamma\alpha}$				-24.4(9.6)				-6(22)	
$G^{(2)}_{\epsilon\delta\alpha}$				-6.9(5.6)				-23(19)	
$G^{(2)}_{\delta\gamma\beta}$				50.2(6.8)				-13(27)	
$G^{(2)}_{\epsilon\gamma\beta}$				59.9(6.0)				-65(22)	
$G^{(2)}_{\epsilon\delta\beta}$				52.7(7.2)				-63(20)	
$G^{(2)}_{\epsilon\delta\gamma}$				36.1(6.1)				-58(18)	
$D_{\beta\gamma\alpha}$[a]	-43.386	14.8(9.8)		9.2(3.9)					
$D_{\beta\delta\alpha}$[a]	2.7384	6.0(2.1)		6.9(1.8)					
$D_{\beta\epsilon\alpha}$[a]				11.0(5.1)	7.2462	12.0(4.4)			
$D_{\delta\gamma\alpha}$[a]	4339.4	293(14)		78.7(5.6)					
$D_{\epsilon\gamma\alpha}$[a]				-9.3(5.0)					
$D_{\epsilon\delta\alpha}$[a]				-22.3(2.2)					
$D_{\delta\gamma\beta}$[a]	5386.1	264(13)		60.6(5.2)					
$D_{\epsilon\gamma\beta}$[a]				-19.0(4.6)					
$D_{\epsilon\delta\beta}$[a]				-27.7(2.4)					
$D_{\epsilon\delta\gamma}$[a]				-53.2(2.7)					
$\upsilon_{ne}D_{\beta\gamma\alpha}$									54(17)
$\upsilon_{ne}D_{\beta\delta\alpha}$									51(15)
$\upsilon_{ne}D_{\beta\epsilon\alpha}$									55(17)
$\upsilon_{ne}D_{\delta\gamma\alpha}$									88(24)
$\upsilon_{ne}D_{\epsilon\gamma\alpha}$									-5(21)
$\upsilon_{ne}D_{\epsilon\delta\alpha}$									-20(17)
$\upsilon_{ne}D_{\delta\gamma\beta}$									-12(23)
$\upsilon_{ne}D_{\epsilon\gamma\beta}$									-58(19)
$\upsilon_{ne}D_{\epsilon\delta\beta}$									-57(18)
$\upsilon_{ne}D_{\epsilon\delta\gamma}$									-52(16)
$\chi^2_{\beta\gamma\alpha}$							10.532		
$\chi^2_{\beta\delta\alpha}$							10.9		
$\chi^2_{\beta\epsilon\alpha}$							8.724		
$\chi^2_{\delta\gamma\alpha}$							15.221		
$\chi^2_{\epsilon\gamma\alpha}$							0.065554		
$\chi^2_{\epsilon\delta\alpha}$							1.4067		
$\chi^2_{\delta\gamma\beta}$							0.23876		
$\chi^2_{\epsilon\gamma\beta}$							8.3928		
$\chi^2_{\epsilon\delta\beta}$							10.248		
$\chi^2_{\epsilon\delta\gamma}$							10.481		

Continued on the next page

TABLE S9 (continued)

	GRASP		AMBiT		Ref. [3]		Fit		
	Cal.	Exp.	Cal.	Exp.	Cal.	Exp.	Linear	QFS	New boson
$s_{\beta\gamma\alpha}$							3.2454σ		
$s_{\beta\delta\alpha}$							3.3015σ		
$s_{\beta\epsilon\alpha}$							2.9536σ		
$s_{\delta\gamma\alpha}$							3.9014σ		
$s_{\epsilon\gamma\alpha}$							0.25604σ		
$s_{\epsilon\delta\alpha}$							1.1861σ		
$s_{\delta\gamma\beta}$							0.48863σ		
$s_{\epsilon\gamma\beta}$							2.897σ		
$s_{\epsilon\delta\beta}$							3.2012σ		
$s_{\epsilon\delta\gamma}$							3.2375σ		

[a] At $m_\phi = 1$ eV. Values over different m_ϕ's are shown in Fig. S16

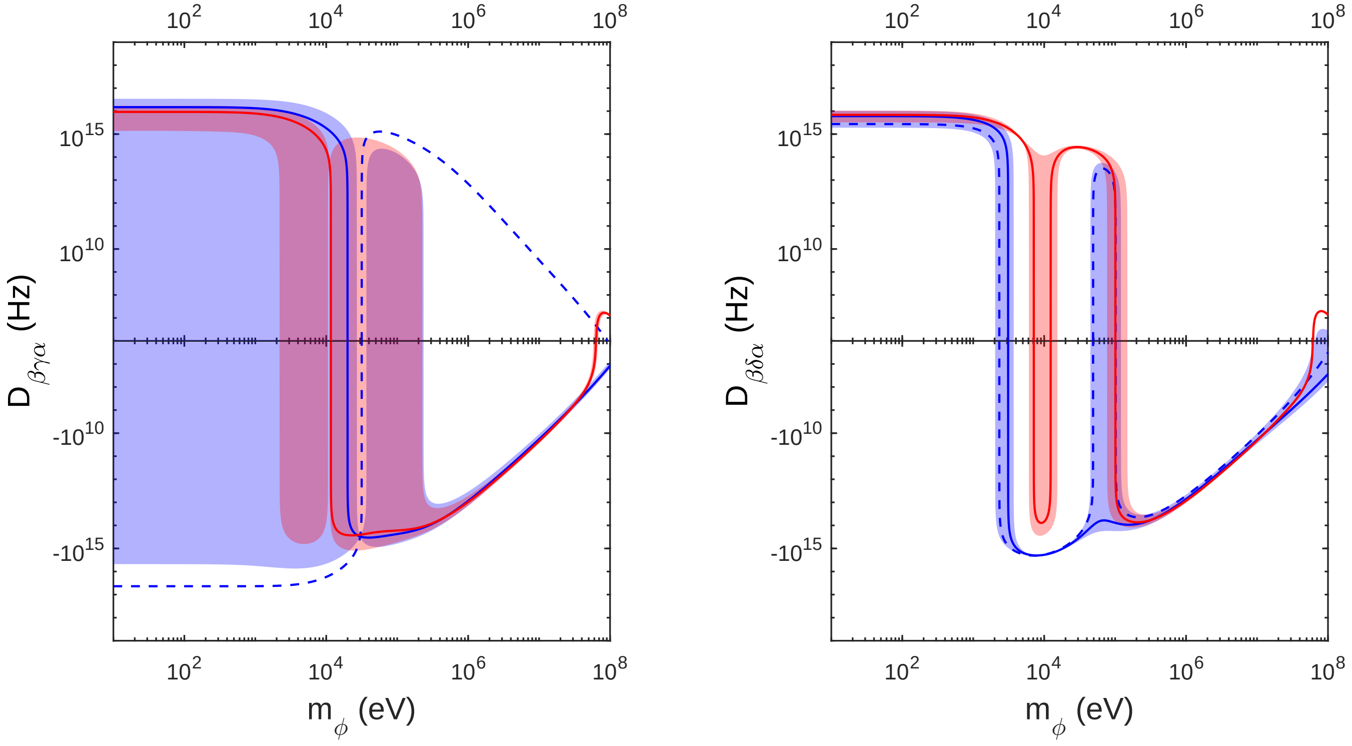

(a) (α, γ, β) transitions

(b) (α, δ, β) transitions

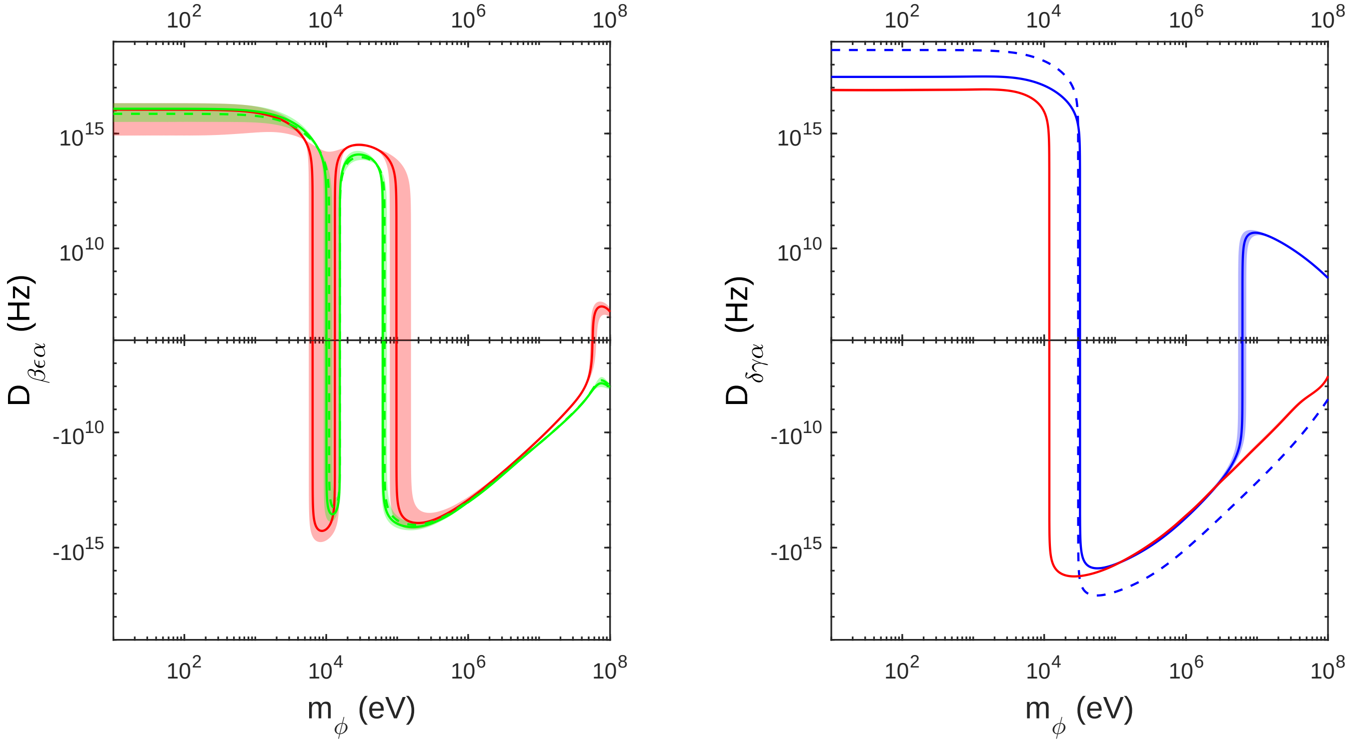

(c) $(\alpha, \epsilon, \beta)$ transitions

(d) (α, γ, δ) transitions

FIG. S16. Calculated $D_{\eta\kappa\chi}$ vs new-boson mass m_ϕ for all different choices of three transitions (χ, κ, η) out of five available transitions α, β, γ, δ, and ϵ, each corresponding to one of the subfigures (a – j). Solid lines correspond to the $D_{\eta\kappa\chi}$ obtained from $D_{\kappa\chi}$ and $D_{\eta\chi}$ in Fig. S15, and $f_{\eta\chi\kappa} = G^{(4)}_{\eta\chi}/G^{(4)}_{\kappa\chi}$ ratio from the linear fit in 3D King plot (see Table S9). Shaded regions for $D_{\eta\kappa\chi}$ indicate 95% confidence intervals that arise from fitted $f_{\eta\chi\kappa}$'s uncertainty. (Figures and caption continue on the next page.)

(e) $(\alpha, \gamma, \epsilon)$ transitions

(f) $(\alpha, \delta, \epsilon)$ transitions

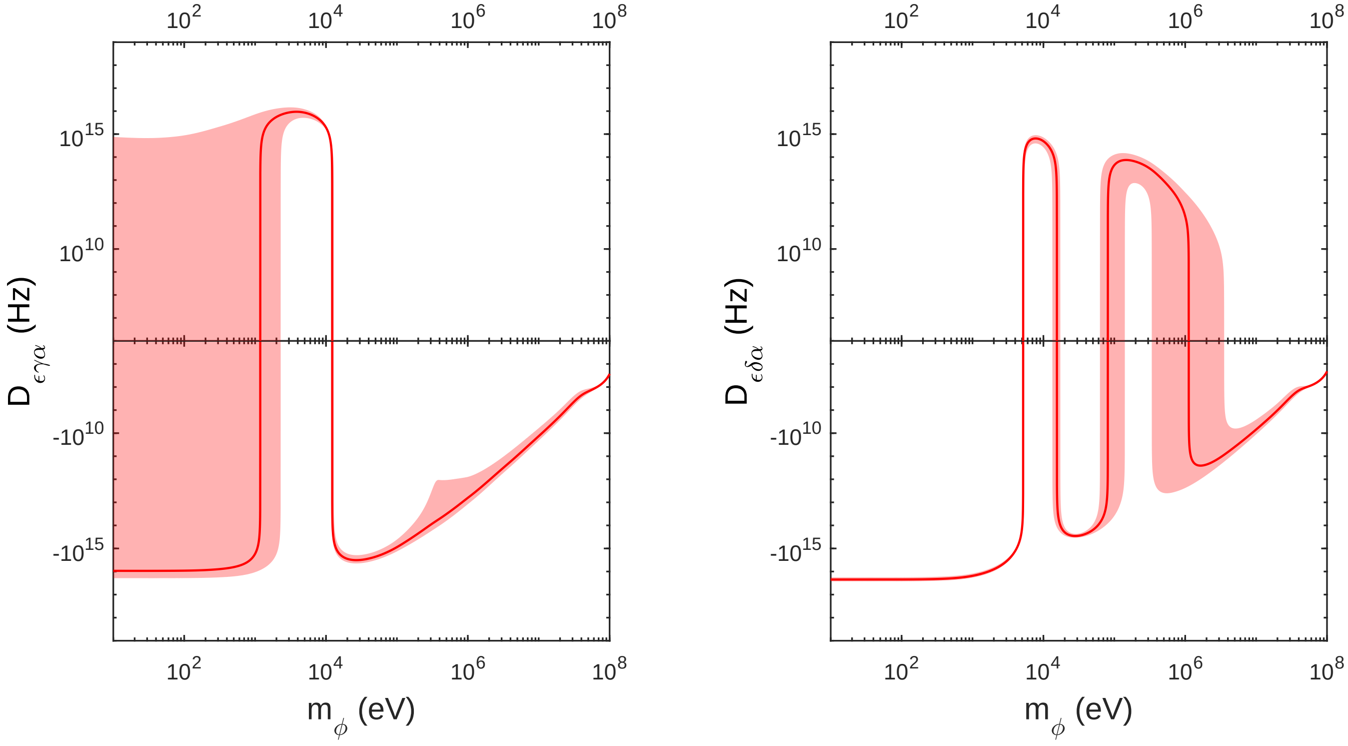

(g) (β, γ, δ) transitions

(h) $(\beta, \gamma, \epsilon)$ transitions

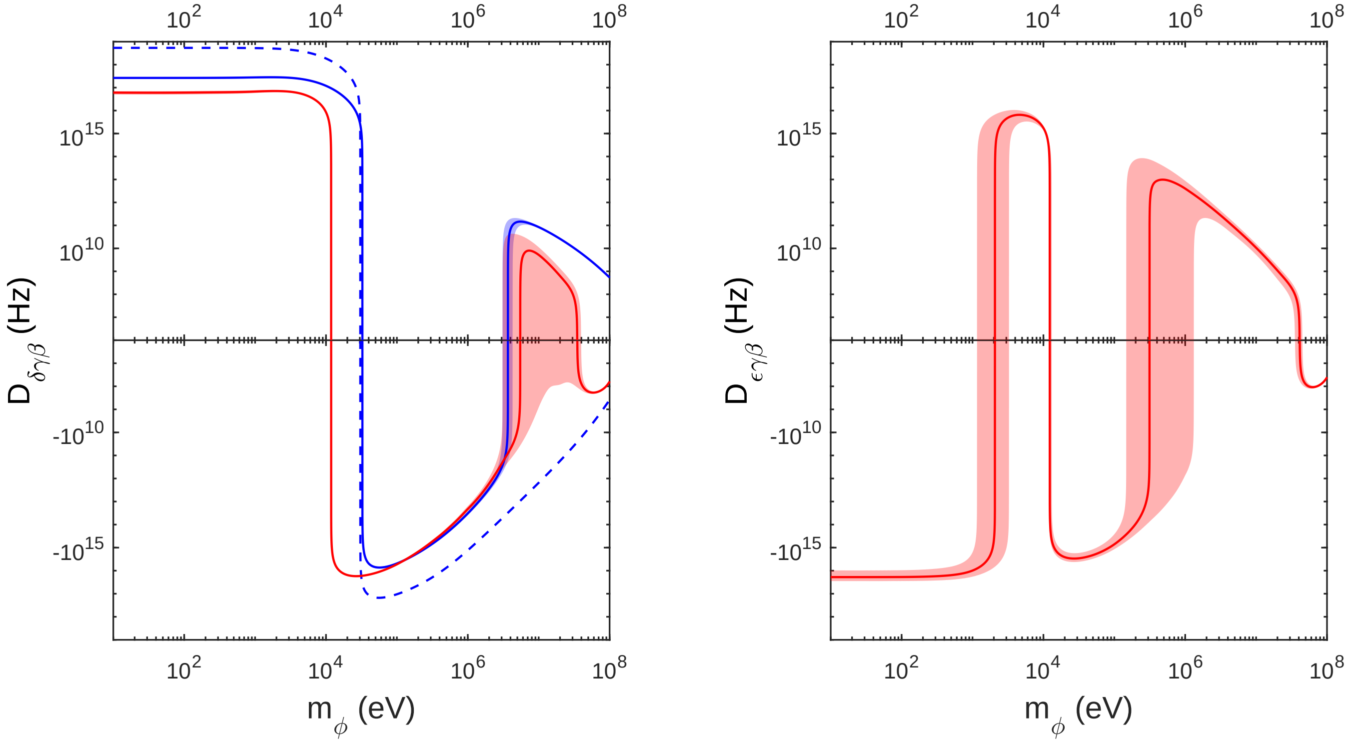

FIG. S16. (Continued) Dashed lines show $D_{\eta\kappa\chi}$ calculated purely from ASCs (i.e., using calculated $f_{\eta\chi\kappa}$). Blue, red, and green colors correspond to ASCs performed using GRASP2018, AMBiT, and in Ref. [3], respectively. (Figures continued on the next page.)

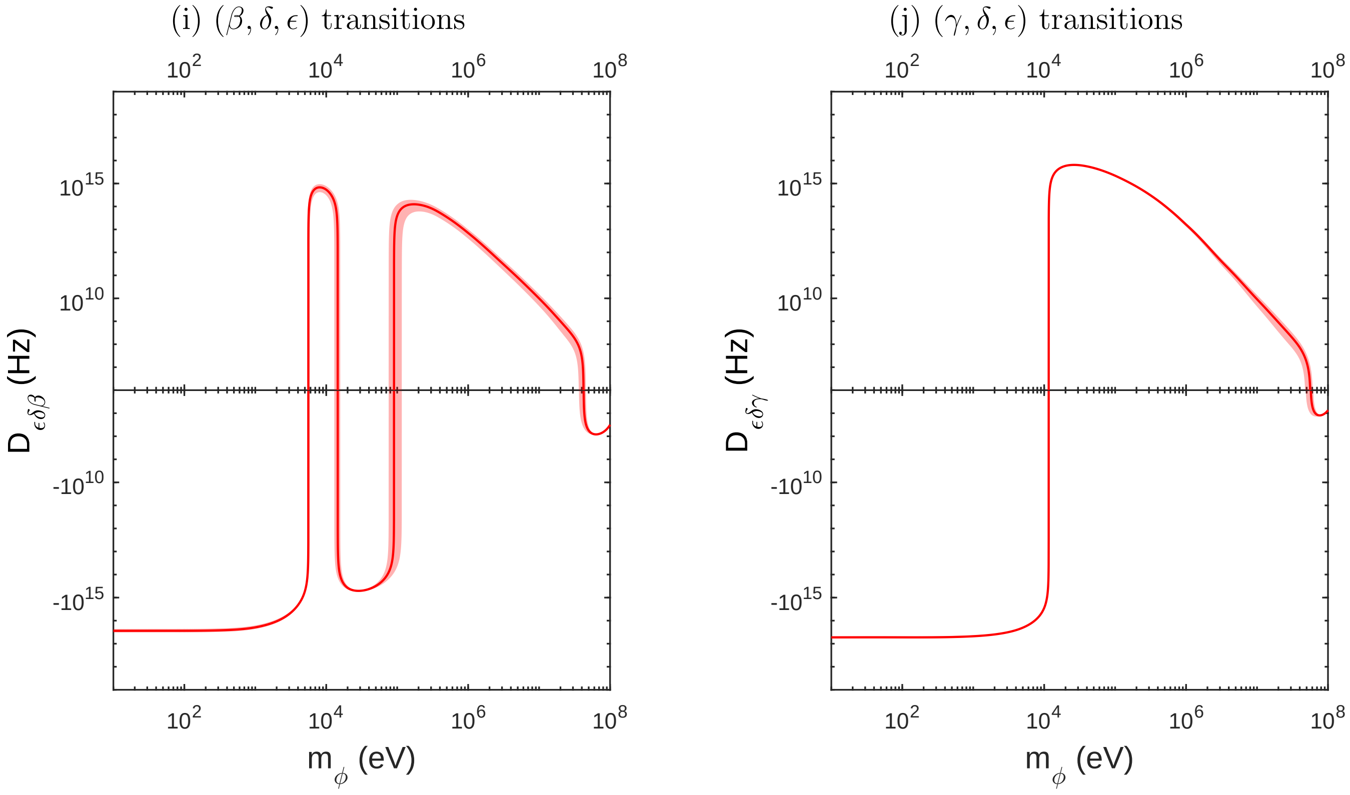
(i) $(\beta, \delta, \epsilon)$ transitions

(j) $(\gamma, \delta, \epsilon)$ transitions

FIG. S16. (Continued)